J. Fluid Mech. (1998), *vol.* 376, *pp.* 221–261. Printed in the United Kingdom

Complex flow mechanisms in compound meandering channels with overbank flow

By K. SHIONO[1] AND Y. MUTO[2]

[1] Department of Civil and Building Engineering, Loughborough University, Loughborough, Leicestershire, LE11 3TU, UK

[2] Ujigawa Hydraulics Laboratory, DPRI, Kyoto University, Kyoto 612, Japan

(Received 21 July 1997 and in revised form 14 July 1998)

Turbulence and secondary flow measurements were undertaken using a two-component laser-Doppler anemometer in meander channels with straight flood plain banks. The most interesting feature of the compound meandering channel flow was found to be the behaviour of the secondary flow. The difference in direction of rotation of the flow before and after inundation at a bend section was confirmed by the detailed velocity measurements. In addition, by performing the measurement over a half wavelength of meander, the originating and developing processes of the secondary flow were also clarified. In contrast to the centrifugal force for inbank flow, the interaction between the main channel flow and the flood plain flow in the cross-over region was found to play an important role in developing a shear produced secondary flow in the overbank cases. New experimental evidence concerning the spatial distribution of Reynolds stress $-\rho\overline{uw}$, $-\rho\overline{uv}$ and $-\rho\overline{vw}$ are presented for sinuous compound meander channels. In such channels, large interfacial shear stresses were induced at around the bankfull level, especially in the cross-over region, and were found to be larger than the bed shear stress in magnitude. Particular importance is placed on $-\rho\overline{vw}$, which is usually small compared with other stress components, as the cause of the secondary flow in the lower layer. The influence of secondary flow on eddy viscosity was found also to be significant. These turbulence data are particularly useful in understanding the flow mechanisms that occur in meandering channels and in developing proper turbulence models for such flows.

1. Introduction

River flows in a compound channel often inundate the adjacent plains at high discharges. This generates a complicated flow structure through the interaction between the main channel flow and the flood plain flow. In straight compound channels, the velocity difference between the flow in the main channel and that on the flood plain is one of the most distinctive characteristics. This introduces several physical and phenomenological features around the junction between the main channel and the flood plain, namely, forming a high horizontal shear layer, streamwise and vertical vortices, momentum transfers and velocity retardation and acceleration. Sellin (1964) identified the existence of vertical vortices at the junction using a flow visualization technique. Zheleznyakov (1965) suggested that the additional flow resistance results from the momentum exchange and called this phenomenon the 'kinematic effect'. The existence of vertical vortices and larger scale lateral movement of the fluid on the flood plain has also been observed by Tamai, Asaeda & Ikeda (1986), Fukuoka & Fujita (1989) and Imamoto, Ishigaki & Muto (1991). There also exist

	Angle of arc (deg.)	Meander wavelength L_w (mm)	Width of meander B_w (mm)	Cross-over length L_{co} (mm)	Cross-over angle (deg.)	Sinuosity s
R1-rectangular	60	1502	452	376	30	1.0930
R2-rectangular	120	1848	900	376	60	1.370
R3-rectangular	180	1700	1000	0	90	1.571

TABLE 1. Meander parameters for tested channels with total width $B = 1200$ mm, bend radius $r_c = 425$ mm, channel width $b = 150$ mm, flood plain height $H = 53$ mm and channel sidewall $s_w = 0$.

strong secondary flows from the edge of the junction towards the water surface of the main channel (Imamoto & Kuge 1974; Shiono & Knight 1989; Tominaga & Nezu 1991).

Much less information is available for compound meander channel flows than for straight compound channel flows. Velocity measurements for compound meander channels have been conducted by: Toebes & Sooky (1967) with a Prandtl tube; Sellin, Ervine & Willetts (1993) with a propeller current meter; Stein & Rouvé (1988), Kiely (1989) and Shiono & Muto (1993) with a laser-Doppler anemometer (LDA). They observed that the primary velocity within the main channel below the bankfull level tends to follow the meander channel, whereas above the bankfull level it tends to follow in the valley direction. Toebes & Sooky (1967) reported that the rotating direction of the dominant secondary cell at the apex in the overbank case is opposite to that in the inbank case. They suggested, from observations at the cross-over section, that this dominant cell at the bend apex is created by the impinging flood plain flow from the upstream side as it flows over and into the main channel. This was also observed by Stein & Rouvé (1988) and Shiono & Muto (1993). They suggested that the difference is not only in the structure, but also in the originating mechanism of secondary flows between inbank and overbank cases. On the other hand, Imamoto, Ishigaki & Fujisawa (1982) and Shiono *et al.* (1994) carried out experiments on a meander channel with meandering flood plain walls and reported that the dominant cell for the overbank case rotated in the same direction as that for the inbank case. This clearly indicated the effect of the phase of the meandering flood plain walls on the secondary flow structure.

A recent research programme on the SERC Flood Channel Facility (SERC-FCF, Phase B) in the UK successfully illustrated the general structures of mean flow, secondary flow and shear flow in compound meander channels (e.g. Sellin *et al.* 1993; Ervine, Sellin & Willetts 1994). Despite the achievements, the SERC-FCF Phase B programme was undertaken for limited ranges of experimental conditions, in particular there was a lack of detailed turbulence measurements along the meander channels. Turbulence measurements have been carried out by Kiely (1989) using a one-component LDA system but he was not able to measure shear stresses and secondary flow directly because of the use of a one-component LDA. We attempted to measure secondary flows and shear stresses directly in the main channel using a two-component laser-Doppler anemometer (LDA) system. This paper presents detailed measurements of secondary flows and Reynolds stresses in the meander channel with straight flood plain banks for overbank flow.

2. Experimental apparatus and instrumentation

The experimental flume was made of Perspex with a rectangular cross-section, whose dimensions were 10.8 m length, 1.2 m width and 0.33 m depth. The longitudinal slope (valley slope) of the flume was set at $0.001 \pm 0.8\,\%$ throughout the measurements. A series of meanders was constructed in the experimental flume. There were 5 meander waves constructed for the cases of $s = 1.370$ and 1.571 and 6 for the case of $s = 1.093$ where a sinuosity, s, is defined as the ratio of the meandering channel length to the meander wavelength. The configurations of the channels used are shown in figure 1 and table 1. The test section for measurements was set in the half meander wavelength of the fourth meander for the $s = 1.370$ and 1.571 cases and in the fifth meander for $s = 1.093$. The test section was divided into 13 or 9 cross-sections and the measurements were undertaken at every other section, i.e. 7 or 5 cross-sections, respectively (see figure 1).

A TSI two-component fibre optic LDA system was employed to undertake velocity and turbulence measurements. The system consists of a 10 m long fibre optic cable connecting the laser and signal processing system (TSI model IFA550) to a 15 mm diameter submersible measurement probe head. The probe head was mounted on a TSI two-axis traverser system which covered 0.6 m in both transverse and vertical directions with a resolution of 0.1 mm.

Because the LDA system was a two-component one, measurements had to be repeated for each point at least twice with different laser beam installations so that all three components of velocity could be obtained. When measuring the streamwise and lateral components of velocity, the probe head was set above the measuring point. It was either in air above the water surface, or submerged, depending on the depth condition. When it was required to measure the vertical velocity component, a 20 mm diameter cylindrical tube with a 45° angle mirror was mounted on the probe head and submerged (figure 2). The laser beams were then coming from either a lateral or downstream position relative to the measuring point depending on the flow and measurement conditions so that the measurement volume was out of the wake of the probe. The definitions of the velocity measurement grids were every $0.1\,h$ (~ 5 mm) vertically and $0.1\,b$ (~ 15 mm) laterally for the main channel (where h and b are the channel depth and the channel width, respectively). Vertical component measurements with the mirror mounted on the probe head were not applicable to the points within 18 mm of the flume bed, owing to the thickness of the mirror tube sole. On the flood plain, the measurement grids were much coarser, being every 1 cm in the vertical direction and every 10 cm in the transverse direction for $Dr = 0.50$ where a relative depth, $Dr[=(H-h)/H]$, is defined as the ratio of the flood plain water depth to the main channel water depth. These were chosen because the secondary flow structure in the main channel, and the shearing mechanisms between the main channel and the flood plain, were of particular interest.

For each point in the main channel, two-component simultaneous measurements were performed at least twice in different laser beam installation modes. One was the mode for the measurement of the streamwise/longitudinal (x; u) and lateral/transverse (y; v) components, the other was that for the streamwise and vertical (z; w) components. The stress tensor components of $\overline{uv}$ and $\overline{uw}$ were obtained, respectively, as products of the fluctuations of the velocity components. In addition, measurements for $\overline{vw}$ were also conducted at 3 or 5 cross-sections in the cross-over section for rectangular channel cases (section numbers 3, 5 and 7 for $s = 1.093$; 5, 7 and 9 for $s = 1.370$; 3, 5, 7, 9 and 11 for $s = 1.571$). The direction along the meander channel wall was defined as the

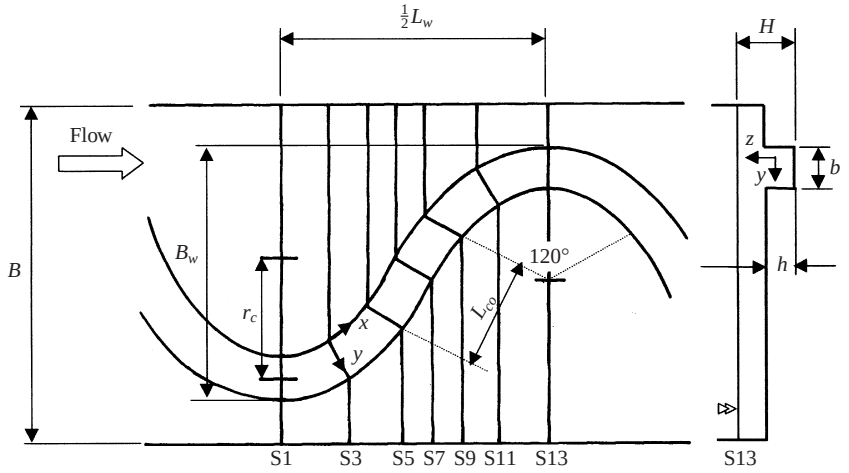

$s = 1.370$, rectangular channel

FIGURE 1. Meandering channel configurations for test section.

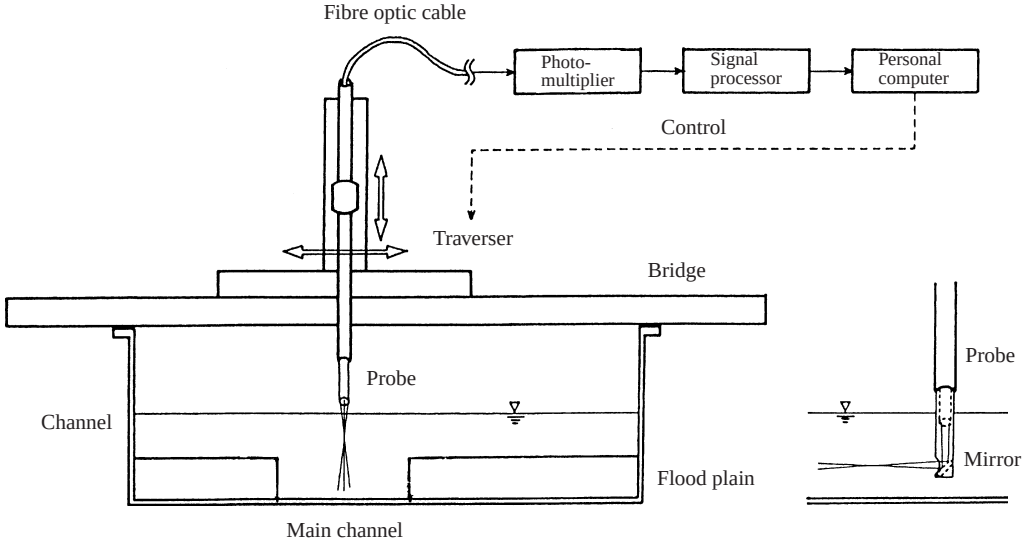

FIGURE 2. Laser beam installations and signal processing system.

streamwise coordinate x, and that perpendicular to x as the lateral coordinate y (see figure 7). An ordinary Cartesian coordinate was adopted for the flood plain, where the longitudinal direction parallel to the straight flood plain wall was defined as the coordinate x. No vertical turbulence measurements were carried out on the flood plain.

It is generally recognized that it is not necessary to employ a seeding agent for LDA measurement in water flows, if using high-power LDAs (Nezu & Nakagawa 1993), since water contains minute particles or materials which can work to scatter the laser beams. However, when trying without any agents, it was difficult to detect the product of two velocity components (i.e. Reynolds stress). This was due to the relatively low laser power of the system. Consequently, it was decided to employ 98% pure aluminium powder, with a 28 μm mean diameter, as a seeding agent. Sampling data

rates with the seeding agent were from 30 Hz to over 200 Hz depending on the flow condition and the measurement location, and the average value was about 100 Hz. It was decided, based on Nezu & Nakagawa's analysis, that a measurement condition of 60 s duration and 100 Hz sampling rate was sufficient for the turbulence measurements in these meander channels.

All the measurements were carried out under quasi-uniform flow conditions. Theoretically, a steady uniform flow condition is defined as $\partial/\partial t = 0$ and $\partial/\partial x = 0$. Physically, the second condition is normally achieved by setting the water surface slope parallel to the bed slope. However, such a condition is impossible to establish in meander channels because of irregular geometries. Thus, as an alternative, the pseudo water-surface slope was determined from measured water depths at the centres of the middle of the cross-over sections. Points within 2 m of both the inlet and outlet of the flume were eliminated from this slope estimation. A pointer gauge with a minimum scale accuracy of 0.1 mm was used for water depth measurements. When the deviation of the pseudo water-surface slope from the bed slope became less than 2%, it was considered to have attained a quasi-uniform flow condition. The deviations of discharge for most cases were within $\pm 5\%$. The setting-up of the water depth was achieved within a $\pm 1\%$ variation for most conditions. These variations were considered to be acceptable, such that the measurements over several days for a given test requirement were considered to be carried out under the same conditions.

3. Flow visualization on the water surface

A flow visualization technique on the water surface in an open channel is often used to obtain a first sight of flow behaviour. This technique is used to capture and interpret flow behaviour in a natural channel when velocity measurements cannot be undertaken, particularly for overbank flow. In order to compare the difference between the flow structures on the water surface and within a channel, flow visualization on the water surface in the channels was first carried out.

For the flow visualization experiment, just one geometry was adopted, a channel with $s = 1.370$, a meander arc of 120°, and a rectangular cross-section. Depth conditions for flow visualization were 1 inbank case and 4 overbank cases, namely $Dr = 0.15$, 0.20, 0.25 and 0.50. Sawdust painted with aluminium power or 5×5 mm^2 pieces of paper were used for the visualization, and pictures were captured by a 35 mm still camera. The camera was mounted on a bridge constructed over the flume. The position of the camera was 2 m above the flume bed. The test section was illuminated by twelve 60 W fluorescent lamps. Figure 3 shows the visualization results zooming in on the cross-over region for $Dr = 0.15$, 0.20 and 0.25 cases. The exposed time was 0.5 s for $Dr = 0.15$ and 0.25 s for the others. The flows run from left to right.

After inundating the flood plain, but with a relatively shallow flooding depth, i.e. $Dr = 0.15$, the flow running along the main channel still seemed to dominate, such that features were recognizable even on the water surface. As shown in figure 3, the flow from the upstream flood plain, after entering the main channel, suddenly deviated, and was forced to follow a streamwise direction, i.e. the direction along the meandering channel. This feature was most clearly seen in the cross-over region. It was obviously caused by the flow in the main channel, which still ran in the streamwise direction after such a shallow inundation. The flow emerging from the main channel onto the downstream flood plain was also observed. It emerged with direction angles not parallel to the flood plain wall, and kept that direction until re-entering the next channel section. This non-parallel angle of the flood plain flow within the meander belt

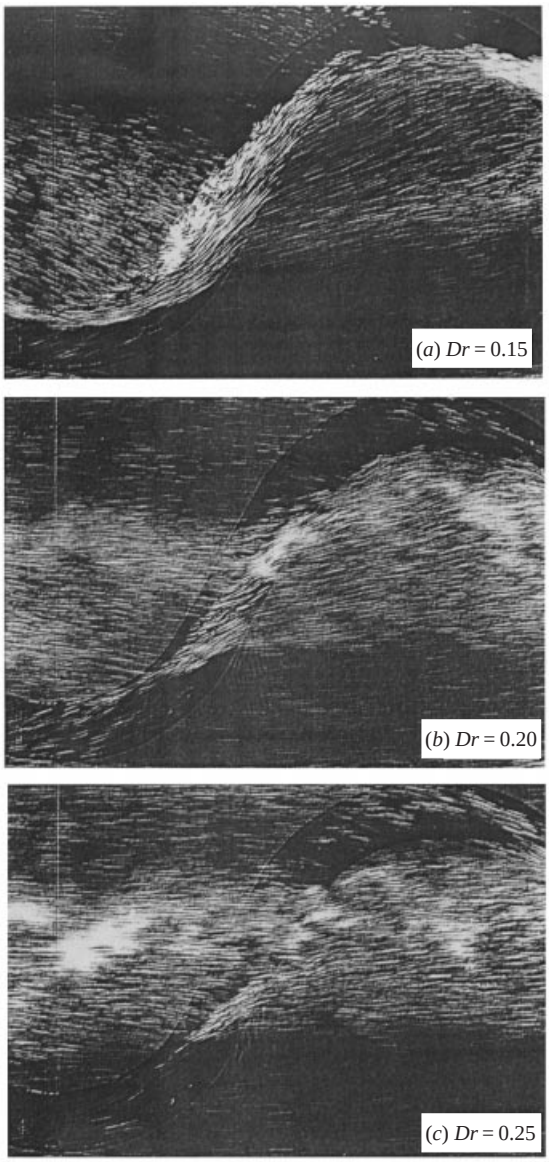

FIGURE 3. Flow visualization on water surface with A1-painted sawdust.

was also a result of the dominance of the channel flow. Elliott & Sellin (1990) show similar flow behaviour of the water surface for overbank flow, using a 9° skew channel in the Phase A SERC-FCF experiments. It was also noticed that fluid motion like eddy trains was formed along the area of the flow deviation. This is probably a feature similar to that reported by Utami & Ueno (1991).

These aforementioned features varied as the flooding depth increased further. When Dr became larger, at 0.25, the deviation was only seen to occur near the entrance and exit of each bend, in a much lesser form than that for $Dr = 0.15$. Though the flow emerged from the main channel in a similar manner as described above for the $Dr = 0.15$ case, it recovered to become parallel to the flood plain wall after some distance on the flood plain. For $Dr = 0.50$, the streamlines on the water surface were almost wholly

aligned in the longitudinal direction, i.e. the flood plain wall direction, and no characteristics of the interaction between the lower- and the upper-layer flows could be observed.

The flow behaviour on the water surface seen from these visualization experiments indicates that when the flood water depth increases, the distinct features of flow interaction between the main channel meandering flow and the flood plain flow disappear. Willetts & Hardwick (1993) demonstrate the complicated flow structure in the main channel below the bankfull level for overbank flow by using a dye tracer technique. It is therefore not possible to capture totally the internal flow structure in the main channel only for high flood water depths by observing only the water surface behaviour.

4. Primary velocity in two layers

Flows in compound meander channels with overbank flow consist of, in principle, the main channel flow and the flood plain flow. Although the flow is extremely complex, the horizontal imaginary plane at the bankfull level has normally been employed by researchers when considering discharge assessment or applying two-dimensional computational models to compound meander channel flows. As a result, it is appropriate to consider the depth/layer averaged velocity distributions first. The results are shown in figure 4. The solid boundaries were set at $\bar{U} = \bar{V} = 0$ for the calculation, whereas at the free surface it was assumed that $\partial\bar{U}/\partial z = \partial\bar{V}/\partial z = 0$. $\bar{U}$, $\bar{V}$ and $\bar{W}$ are temporal mean values. The lateral axis of the figure is the transverse distance y taken from the left-hand side embankment.

For the bankfull case, figure 4(*a*), the shift of the core region from the inner side of one bend apex to the outer wall can be clearly seen through the latter half of the bend to the cross-over. After proceeding into the cross-over, the velocity vectors are modulated to be parallel to the channel wall. The core region reaches near the inner wall at the entrance of the next bend and goes along the wall up to the apex. This flow pattern is similar to previous studies on curved channels, in which faster flow in the inner side and super-elevation in the water surface appear. This behaviour has been explained through an irrotational flow theory in a curved bend or free vortex motion with a constant circulation.

It can be noticed for $Dr = 0.15$, figure 4(*b*), that the flow velocity becomes slower in both the lower and the upper layer than the bankfull case. It is also observed that the velocities are distributed more uniformly in the lower layer than the bankfull case since the super-elevation in the water surface around a curved channel no longer exists owing to the flood plain flow. The magnitudes of the vectors are longer in the main channel than on the flood plain. The flow outside the meander belt is almost parallel to the flood plain wall, whereas the flow within the meander belt shows some deviations. The deviations originate when the flow leaves the main channel onto the flood plain, as a result of the interaction with the lower-layer flow. After entering the flood plain, the flow tends to keep its deviated angle until it reaches the next channel section. In the region between section 3 and section 11, the primary direction of the upper-layer flow varies gradually from a more or less streamwise direction to a longitudinal direction as it proceeds downstream. This implies that the intruding flow from the flood plain becomes more and more dominant from the cross-over to the first half of the next bend in the upper layer.

It can be noticed that at section 5 there is a significant difference of flow directions in the upper-layer flow either side of the centre of the channel. This location

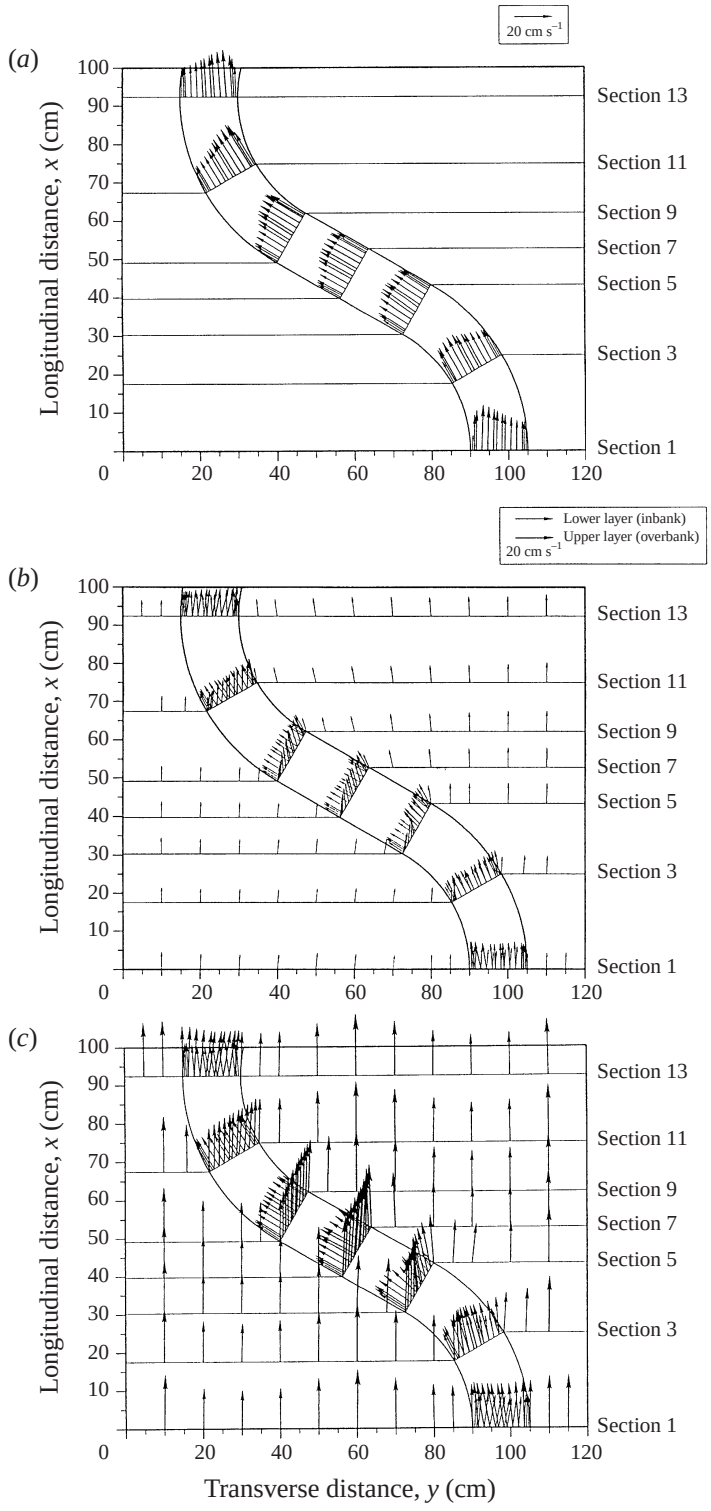

FIGURE 4. Layer averaged velocity distributions in the rectangular channel for $s = 1.37$, (*a*) bankfull, (*b*) $Dr = 0.15$ and (*c*) $Dr = 0.5$.

corresponds well to the area of the eddy train appearance seen in the visualization experiments. This difference is caused by the interaction between the upper- and lower-layer flows which generates vertical vortices as a result of the gradient of the lateral component of velocity.

When the relative depth becomes $Dr = 0.50$, figure 4(*c*), the magnitudes of the velocity vectors in the upper layer are larger than for the lower-layer flow, and their directions are very nearly parallel to the flood plain wall. An outward flow is observed on the flood plain immediately downstream from the concave channel edge and is related to the emerging flow from the channel onto the flood plain. This feature also causes the retardation for the flow within the meander belt as the flow contracts. The exception within the belt is at the centre of the flood plain ($y = 60$ cm at section 11), where the maximum velocity on the flood plain is seen. The lower-layer flow seems to go outwards in the bend from the apex to the exit, as if it is driven by the upper-layer flow to come out of the channel. On the other hand, from the middle part of the cross-over, the velocity distribution becomes more uniform and its primary direction is streamwise. It can be expected from these observations that the flow structure in the lower layer would be significantly changed from the exit of the bend to the cross-over region.

The area of fluid motion like eddy trains which occurs in the cross-over region at a shallow flood depth of $Dr = 0.15$, corresponds to the area where there are large differences in the vector angles between the upper and lower velocity directions (see figure 4*b*). In this region, a large amount of turbulent kinetic energy should be generated by this shearing, as will be discussed later. As the flood water depth becomes deeper, the angle difference between the lower- and upper-layer flows seems to become more constant across the section. This shows that the interaction at the bankfull level is less significant, and that the flows in these layers are less dependent on each other. This agrees well with the data obtained by Sellin *et al.* (1993). They show velocity vectors above and below the bankfull level, along a compound meander channel, for overbank flow. In their results, the velocities in the lower and upper layers follow the meandering channel direction and the floodplain bank direction, respectively, for a deep flood depth case. As a result, the use of a two-layered system dividing at the bankfull level, for estimating the discharge seems to work very well at large flood water depths, but does not work for shallow flood water depths.

5. Streamwise velocity in the main channel

As mentioned in the previous section, there exists some flow interaction at the bankfull level for overbank flow, for low to medium flood plain flow depths. In order to show the interaction at the bankfull level along the whole of the meandering channel, the detailed flow structures within the meandering channel are required and are now described as follows.

Figure 5 shows the cross-sectional distributions of the streamwise velocity along the meander channel for three depths; bankfull, $Dr = 0.15$ and $Dr = 0.5$. The lateral axis represents the lateral distance y normalized by the channel depth at bankfull, h, taking the left-hand sidewall of the channel as the origin. The vertical axis expresses the vertical distance z normalized by h, which is taken from the channel bed. The velocity is normalized by the section averaged velocity $U_s = Q/A$, where Q is discharge and A is the cross-sectional area at the bend apex.

For the bankfull case, figure 5(*a*), the maximum velocity has a magnitude which is over 30 % larger than U_s and is located along the inner wall of the main channel at the

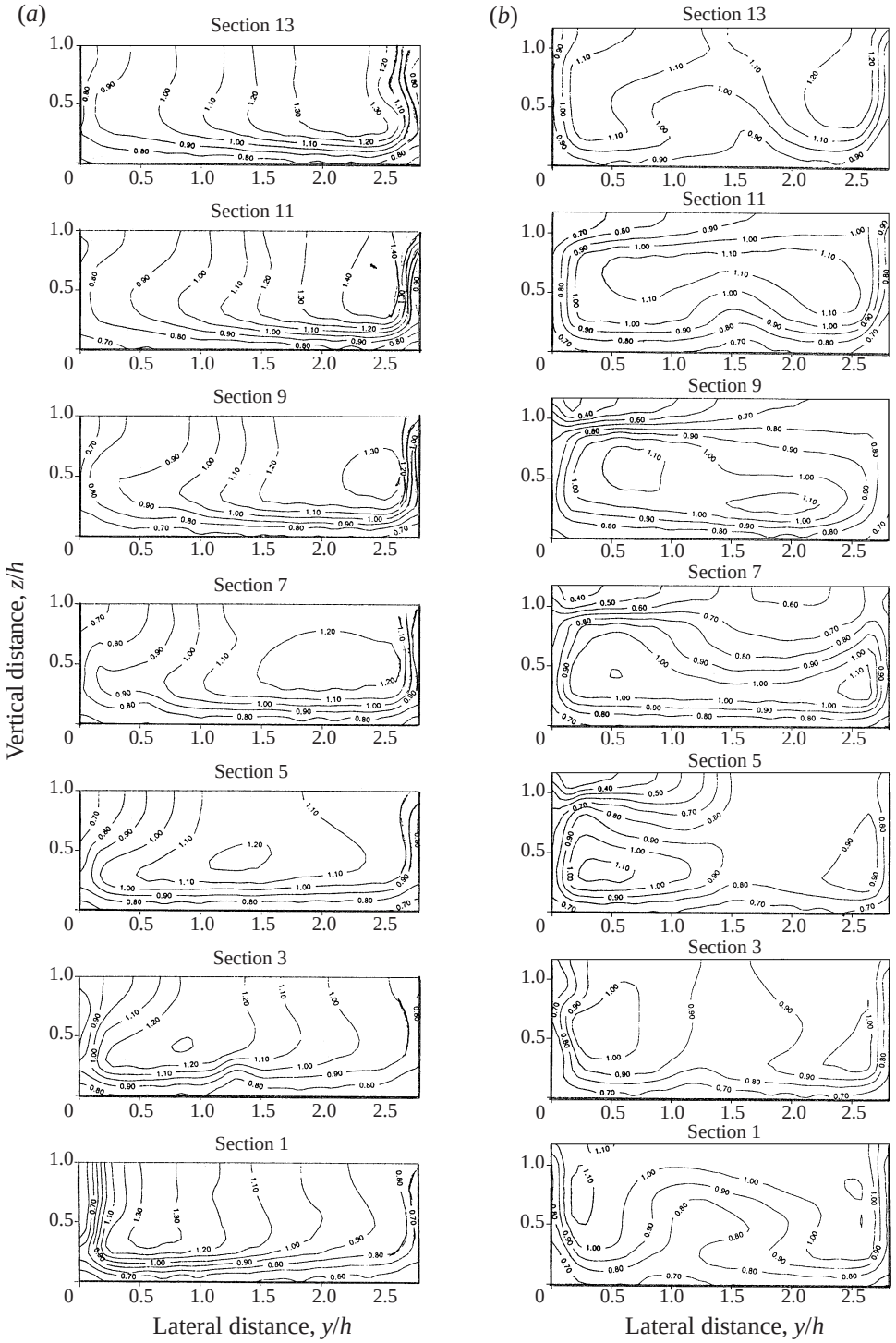

FIGURE 5(*a*, *b*). For caption see facing page.

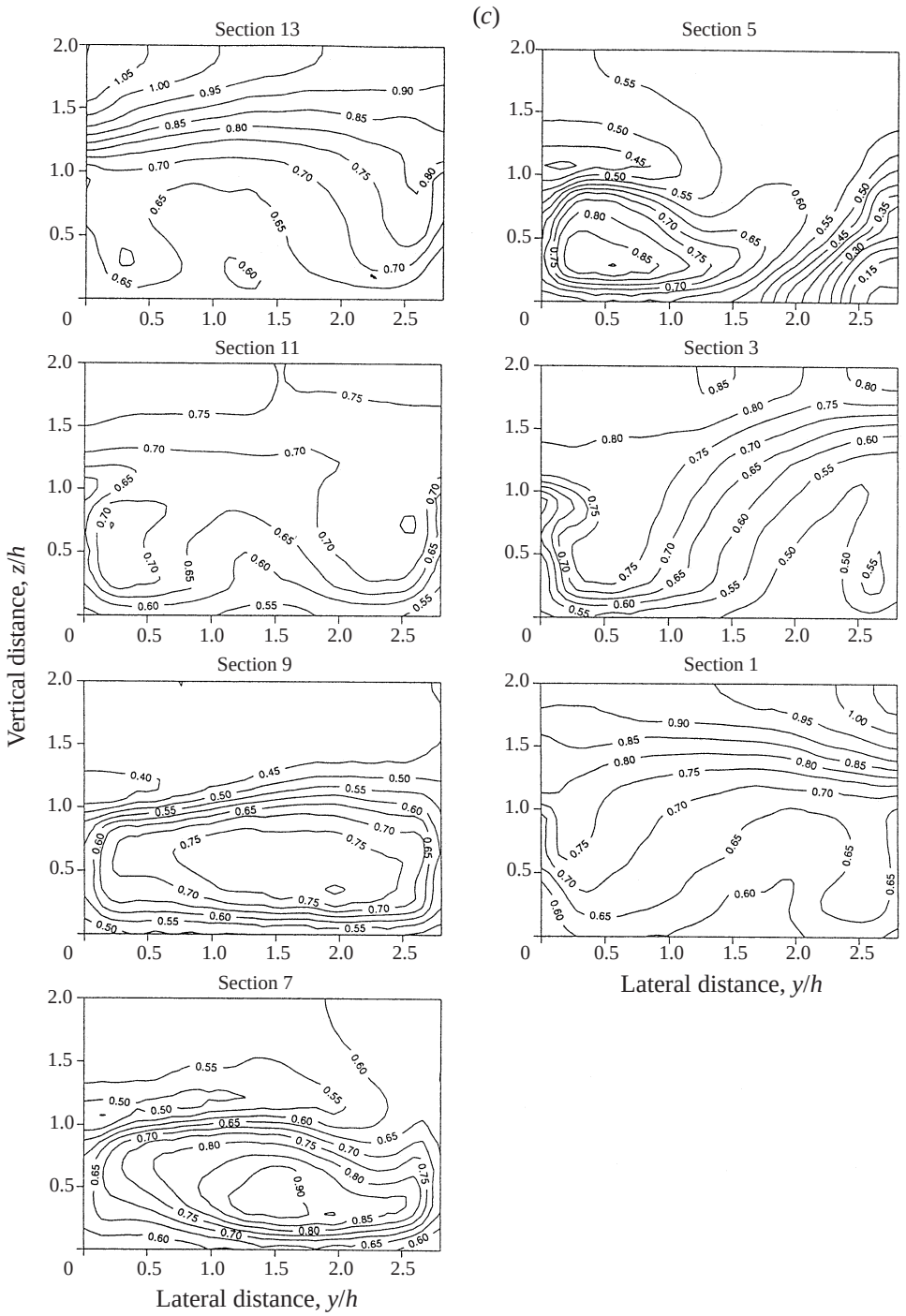

FIGURE 5. Streamwise velocity distributions in the rectangular channel for $s = 1.37$, (*a*) bankfull, (*b*) $Dr = 0.15$ and (*c*) $Dr = 0.5$.

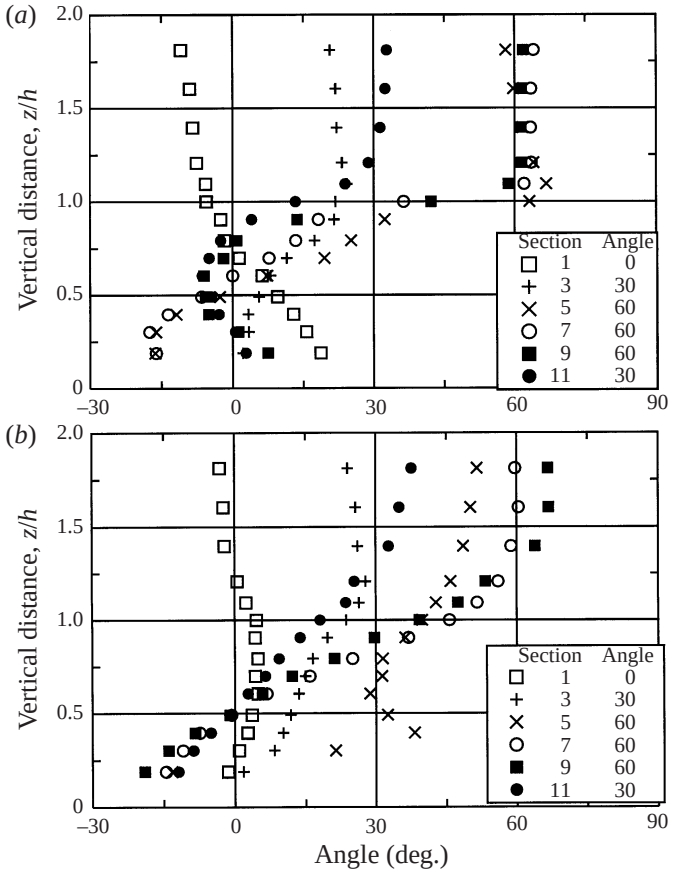

FIGURE 6. Flood flow angle to meandering channel with depth variation for $s = 1.37$ and $Dr = 0.5$, (*a*) $y/h = 0.56$. (*b*) $y/h = 2.55$.

bend apex (section 1). As the flow goes through the latter half of the bend, the core region moves towards the outer wall and the velocity distribution becomes more uniform. In the middle of the cross-over region (section 7), a faster flow region with a velocity 10% larger than U_s reaches the right-hand sidewall and runs along the wall. The maximum velocity over the half meander is then observed to occur at section 11, where it reaches up to 140% or more of U_s. The mirror image of the velocity distributions are attained between the consecutive bend apexes (sections 1 and 13).

For $Dr = 0.15$, figure 5(*b*), it is apparent that faster regions are formed near both channel walls at the bend apex. The central part is occupied by the slower moving fluid from near the bed, driven by secondary flows (see also section 1 in figure 8*b*). No distinct velocity difference is seen at the bankfull level between the channel flow and the flow above that level. However, in the cross-over region (section 5–9), a steep velocity gradient can be seen in the vertical direction from the dense contour lines about the bankfull level. This is due to the flow entering from the upstream flood plain into the main channel. The area which is affected by the intruding flow develops laterally as it proceeds in the cross-over sections as seen in the flow visualization experiments. It should be noticed that good portions of the main channel, over the meander wave and below the bankfull level, have a velocity $\bar{U}/U_s > 1.0$, which suggests that the streamwise flow in the main channel is still dominant.

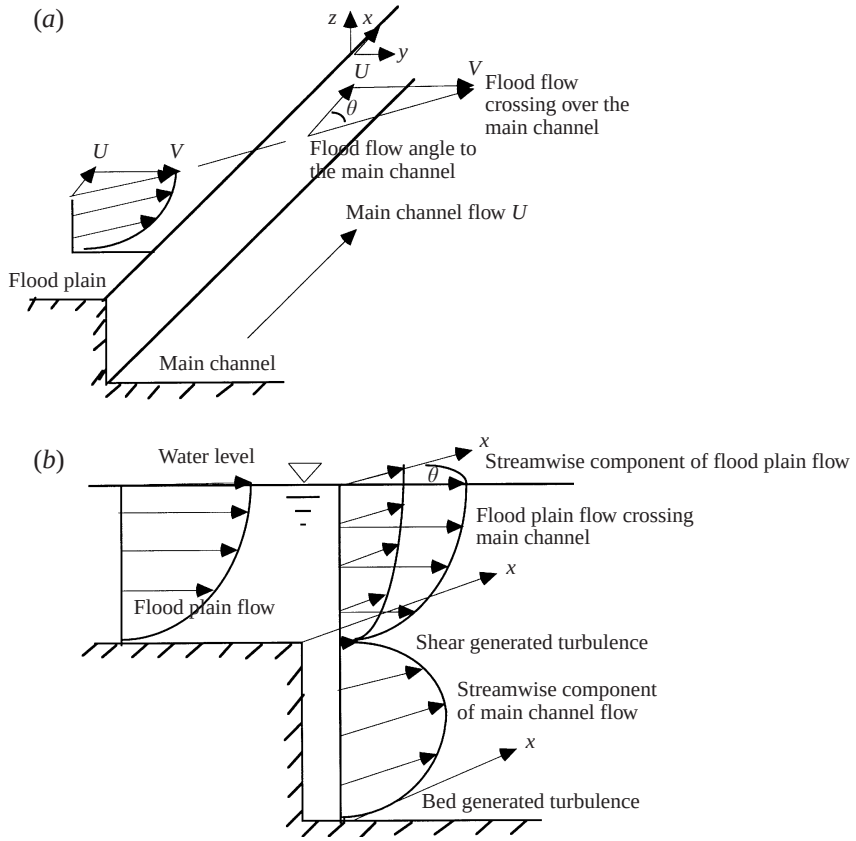

FIGURE 7. Illustration of streamwise components of flood flow and main channel flow.

For $Dr = 0.50$, figure 5(*c*), a steep velocity gradient in the vertical direction is also seen at around the bankfull level in the cross-over region. Other features are: (*a*) an area of slow fluid movement formed along the outer wall of the latter half of the bend (sections 3–5); and (*b*) the flow below the bankfull level having a value of $\bar{U}/U_s$ less than 1.0 throughout the meander. It can be seen in section 9 that the velocity above the bankfull level, $z/h = 1.0$, is more or less uniform since there are no contour lines. There is a strong vertical shear layer at around the bankfull level in the inner side of the channel. The shear layer is generated by the flood plain flow crossing over the main channel flow, and may therefore depend on magnitudes and entering angles of the flood plain flow. An investigation of the angle of the flood plain flow to the meandering channel flow was therefore carried out.

The flood plain flow can be resolved into two components with an angle, θ, where this angle is the angle of the flood plain flow entering the meander channel. The angle, θ, can be estimated using $\theta = \tan^{-1}(\bar{V}/\bar{U})$. Variations of the flood plain flow angle at two locations, taken as $y/h = 0.56$ (inner side of the meander channel) and $y/h = 2.55$ (outer side), are shown in figure 6 as two typical examples. This shows that the angles above the bankfull level in the cross-over region agree with the meander channel angles for most sections at $y/h = 0.56$, although there is slight disagreement in some places. At $y/h = 2.55$, the angles do not coincide with the meander channel angles, particularly at sections 5 and 9. This indicates that the main channel fluid is flowing out into the flood plain. The angles at sections 1, 3 and 5 are less than the channel angles, which

indicates that the flood plain flow is being deflected towards the main channel flow direction by the main channel, but the angles at sections 9 and 11 are larger than the channel angle, indicating that the flood plain flow is deflected outwards towards the flood plain. These features can also be seen in figure 4(*c*). An angle between the meandering channel and the flood plain wall thus controls the magnitude of the streamwise velocity above the bankfull level.

The angle of the meander channel is therefore one of the main parameters generating velocity differences, or shear, between the lower and upper layers at the bankfull level, as shown in figure 7. Another factor controlling the magnitude of the shear is obviously the flood water depth. As the water depth increases, the streamwise component of the flood plain flow in the upper layer increases, and as a result the velocity difference in the cross-over section will be reduced, hence reducing the flow resistance at the bankfull level. In contrast, for a straight compound channel the shear is normally generated by the lateral velocity difference between the main channel and flood plain flows (Knight & Shiono 1990). The shearing mechanisms between a straight compound channel and a meander compound channel with straight flood plain banks for overbank flow are therefore significantly different.

6. Secondary flow structure in the main channel

Sellin *et al*. (1993) illustrate the secondary flow structure along a meandering channel for overbank flow using velocity data, but the vertical component of velocity was not available for their illustration of the secondary flow. In this study, the vertical and lateral components of velocity were both measured and therefore the secondary flows could be investigated. These are described in the following section.

The results for the secondary flow structure are shown in figure 8 in a two-dimensional vector form. Note that each set of these figures has a different vector unit length and this is shown at the bottom of the group. For the bankfull case, figure 8(*a*) shows the growth and decay of the secondary flows through the bend meander. At the apex section, a fully developed single cell is not seen. Following the suggestion by Rozovskii (1961), the angle required for the full development of secondary flows in the tested bend is 220°. Hence, secondary flows can never be fully developed in the test meander channel. This is attributed to the large depth H, relative to the radius of the bend r_c, and hence also the small main-channel aspect ratio. The developing secondary flows seem to reach their maxima in both size and magnitude at the exit of the bend, section 5, where a large clockwise cell can be observed. At the entrance of the next bend, section 9, a dominant flow running from the upper left-hand corner to the lower right-hand one can be seen. This is probably the 'adjusting process' pointed out by Shukry (1950). After proceeding into the next bend, a cell which rotates in an anticlockwise direction starts to develop on the inner side of the channel owing to the centrifugal force, e.g. see section 11. The other cell, which occupies the outer side of the channel at section 13, is the residue of the secondary flow developed through the previous bend. According to the estimate based on Shukry's method (1950), the length required for the cell dissipation in the tested channel is 1.2 m. Consequently, it is likely that such a residue would be observed even in bend sections under the test conditions. This residual secondary flow prevents the development of the secondary flow generated by the centrifugal force in the whole cross-section, normally seen in a wide curved channel. The maximum lateral velocity over the meander wave appears at

section 5 and has a magnitude of 16% U_s. Apart from this section, the magnitude of the lateral velocity is less than 10% U_s over most of the areas. However, these figures are far larger than those observed either in straight channels, 2–3% $\bar{U}_{max}$ (Nezu & Rodi 1986), or in straight compound channels, 4% $\bar{U}_{max}$ (Tominaga & Nezu 1991). The magnitude of the vertical velocity is generally weaker than that of the lateral component in the bankfull flow and less than 4% U_s in most of the area. The areas of relatively high value can be seen in the vicinity of the channel walls, particularly along the inner wall of bends, where the velocity has a positive sense and a magnitude of over 10% U_s.

The $Dr = 0.15$ case, figure 8(*b*), has a dominant cell at section 1 which rotates anticlockwise and is situated near the inner wall. The cell suddenly disappears somewhere in the latter half of the bend, synchronous with the appearance of a new clockwise rotating cell in the upper half along the inner wall from section 3. This new cell immediately grows and occupies most of the cross-section in the cross-over sections. Some parts within the cell show a relatively high-velocity magnitude. It should also be noted that the flow entering from the flood plain into the main channel (plunging flow illustrated by Willetts & Hardwick 1993), and re-entering from the main channel onto the flood plain (escaping flow), can be clearly detected along the top of the outer wall in the latter half of the bend (sections 3 and 5). As it runs into the flood plain, it increases its velocity as if passing through a contraction in a pipe. It is clearly seen that the area above the bankfull level in the cross-over region is occupied by fluid with a high lateral component of velocity of over 30% U_s. The magnitude of the vertical velocity can reach 20–30% U_s, similar to the lateral component, and can become more than 50% U_s along the inner wall of bends ($y/H = 2.5$ in section 11), where the sense is negative. It is also noticeable that a positive area of 25% U_s is observed in the upper part, along the outer wall of the latter half of the bend. These magnitudes depend on the magnitude and the entering angle of the flood plain flow into the main channel.

For the $Dr = 0.50$ case, figure 8(*c*), almost the whole of the cross-sectional area seems to be occupied by one dominant secondary flow cell at the bend apexes. The cell has already disappeared by the next section after the apex and a new cell is formed in the same manner as for the $Dr = 0.15$ case. The cell develops in size as the cross-section proceeds, but it does not involve the upper part of ($z/h > 1.2$). Only at the bend apex does it extend for the first time up to the water surface. The flow shows expansion behaviour as it enters from the flood plain into the main channel and contraction as it leaves again onto the flood plain at sections 3 and 5. However, after the new cell develops in size equivalent to the channel width at section 7, these behaviours cannot be seen, but the flow seems to just travel over the cell in the main channel, sections 7, 9 and 11. This suggests that the contraction and expansion theories along the meander channel are partially correct, as adopted by Ervine & Ellis (1987) in their discharge estimation method, but not for the whole meander channel.

7. Streamwise vorticity

The most important feature of secondary flow structures in meandering channels is the opposite directions of the secondary flow cell rotation at bend apexes before and after inundation and different originating mechanisms for inbank and overbank flows. More detailed analysis of these mechanisms was carried out using the mean vorticity

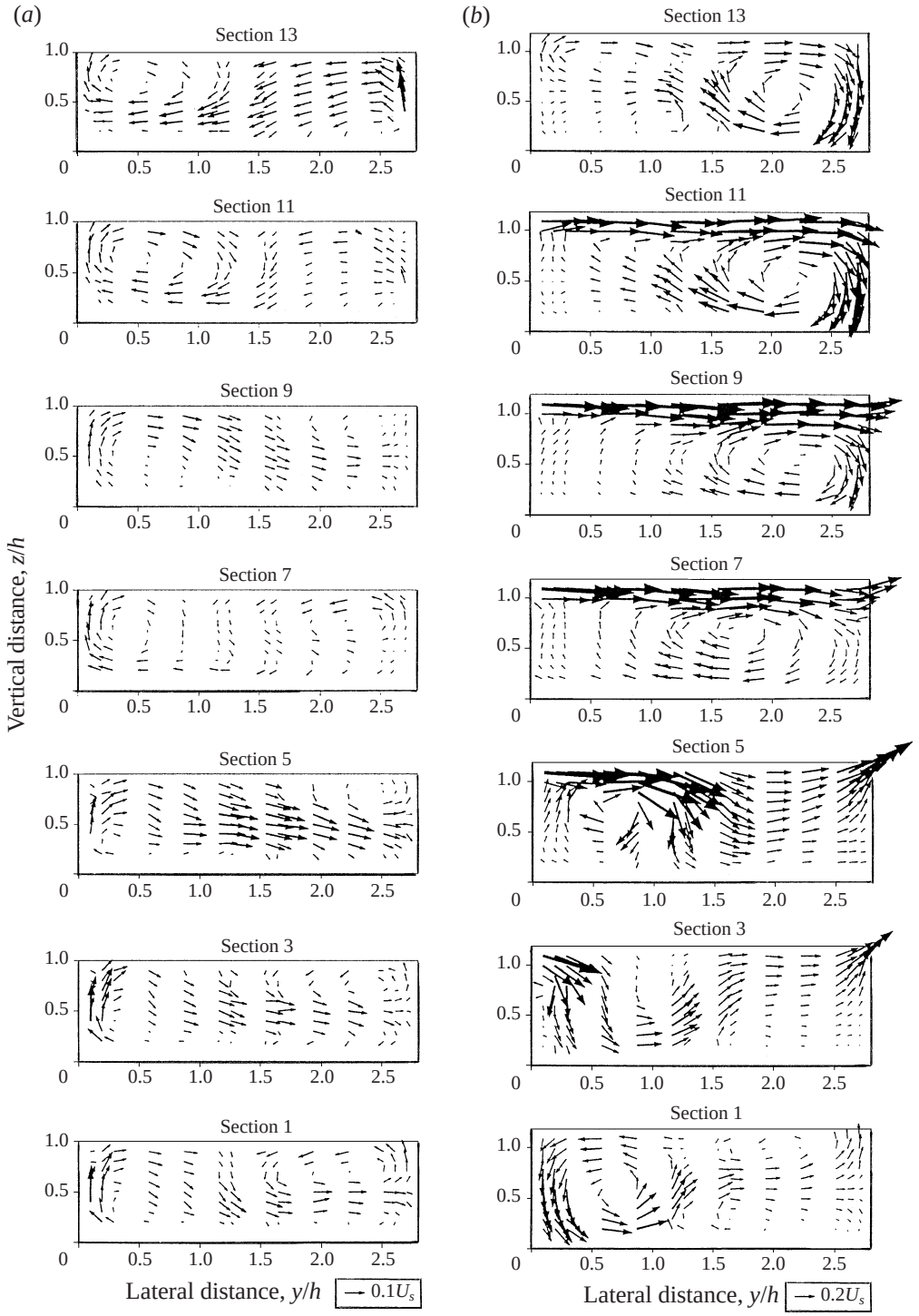

FIGURE 8(*a*, *b*). For caption see facing page.

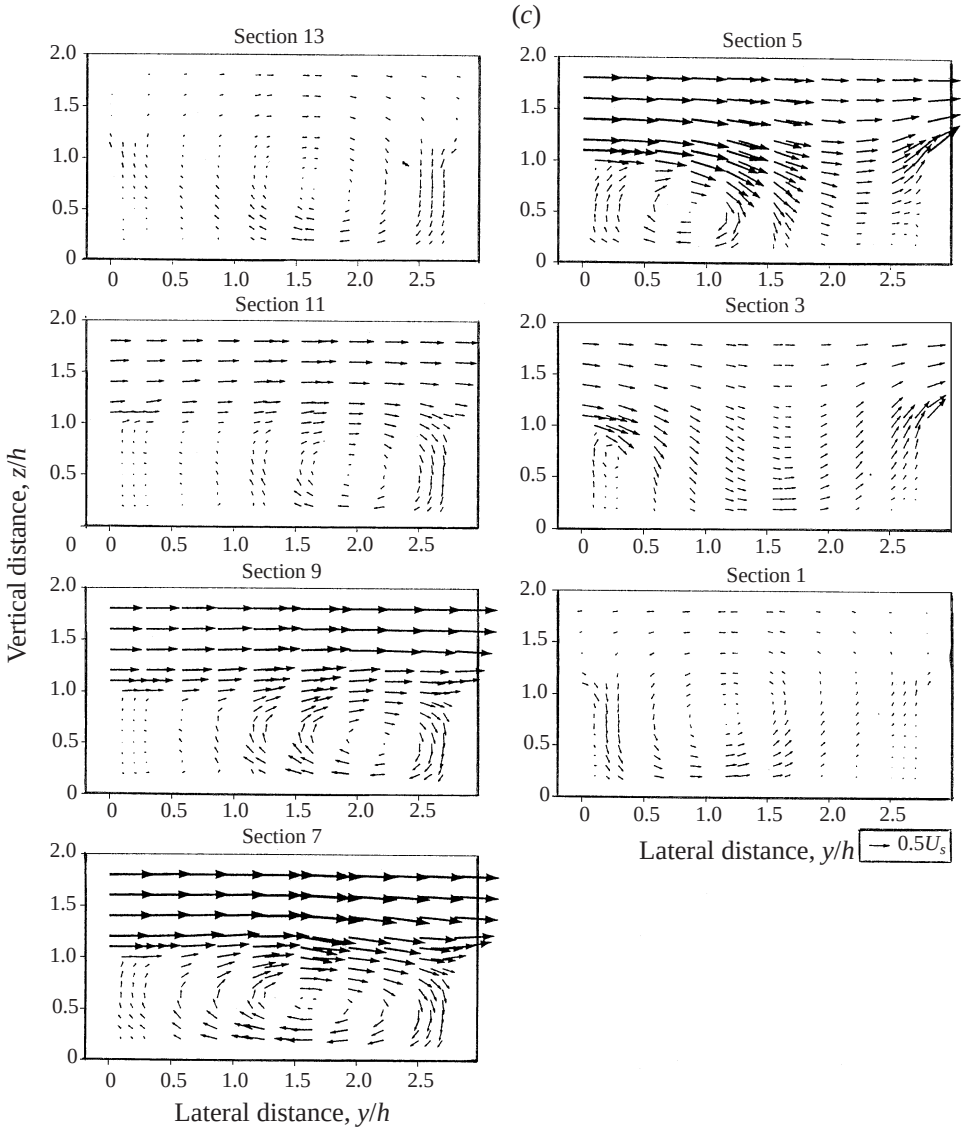

FIGURE 8. Secondary flow vectors for $s = 1.37$, (*a*) bankfull, (*b*) $Dr = 0.15$ and (*c*) $Dr = 0.5$.

transport equation. The mean vorticity transport equation can be written as a tensorial form with alternating tensor ε_{ijk}:

$$\frac{\partial \omega_k}{\partial t} + \overline{U_j}\frac{\partial \omega_k}{\partial x_j} = \omega_j \frac{\partial \overline{U_k}}{\partial x_j} + \nu \frac{\partial^2 \omega_k}{\partial x_j \partial x_j} + \varepsilon_{ijk}\frac{\partial}{\partial x_i}\left(\frac{\partial \overline{(-u_j u_n)}}{\partial x_n}\right). \tag{1}$$

Multiplying by ω_i and noting that $\omega_i^2 = \omega^2$, where ω is the mean magnitude of the mean vorticity vector, lead to the mean vorticity equation

$$\underset{\text{I}}{\frac{\partial \omega^2}{\partial t} + \overline{U_j}\frac{\partial \omega^2}{\partial x_j}} = \underset{\text{II}}{2\omega_k \omega_j \frac{\partial \overline{U_k}}{\partial x_j}} + \underset{\text{III}}{2\nu\omega_k \frac{\partial^2 \omega_k}{\partial x_j \partial x_j}} + \underset{\text{IV}}{\varepsilon_{ijk}\omega_k \frac{\partial}{\partial x_i}\left(\frac{\partial \overline{(-u_j u_n)}}{\partial x_n}\right)}. \tag{2}$$

Term I comprises the temporal and convective change in mean vorticity.

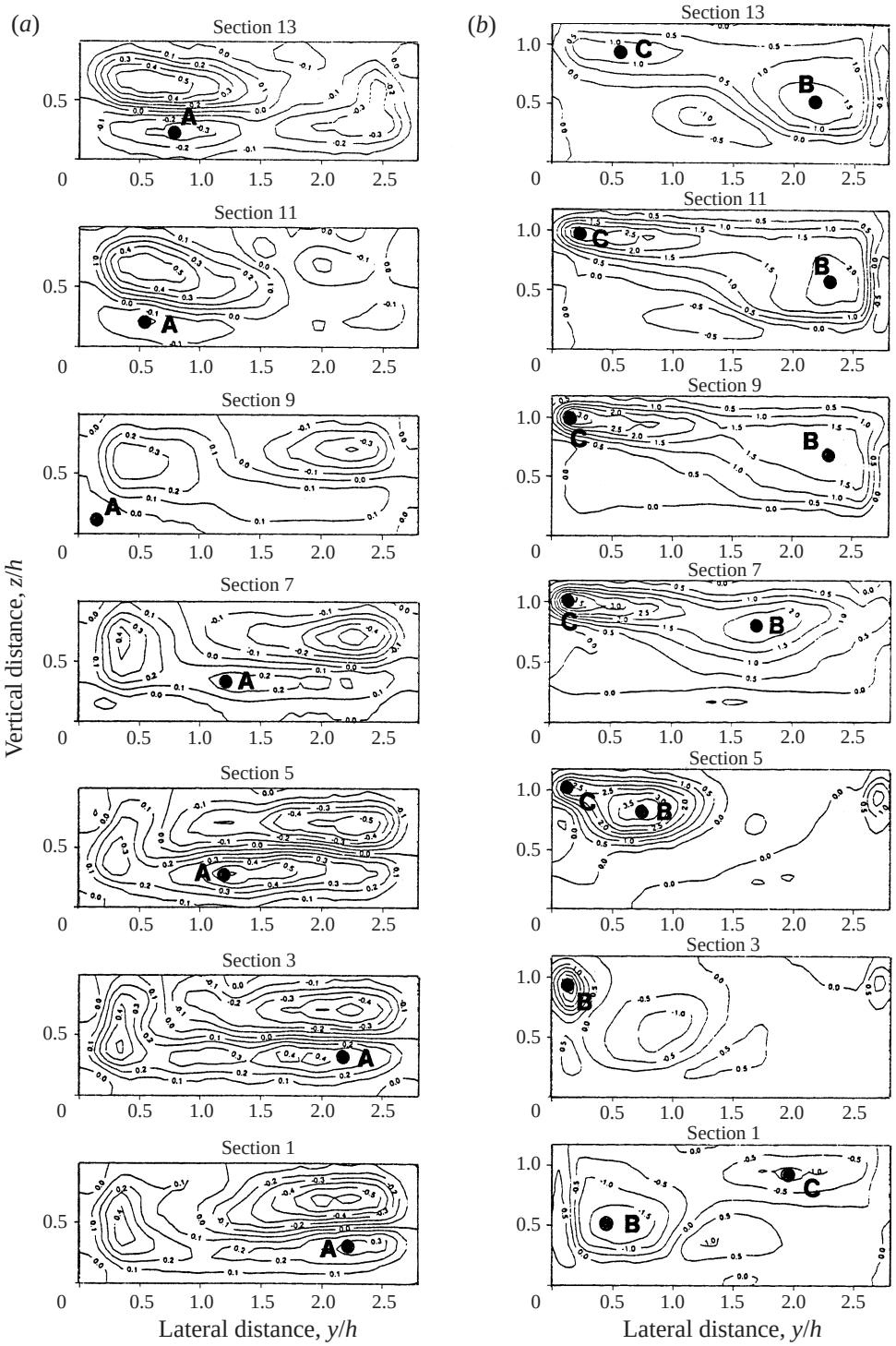

FIGURE 9(*a*, *b*). For caption see facing page.

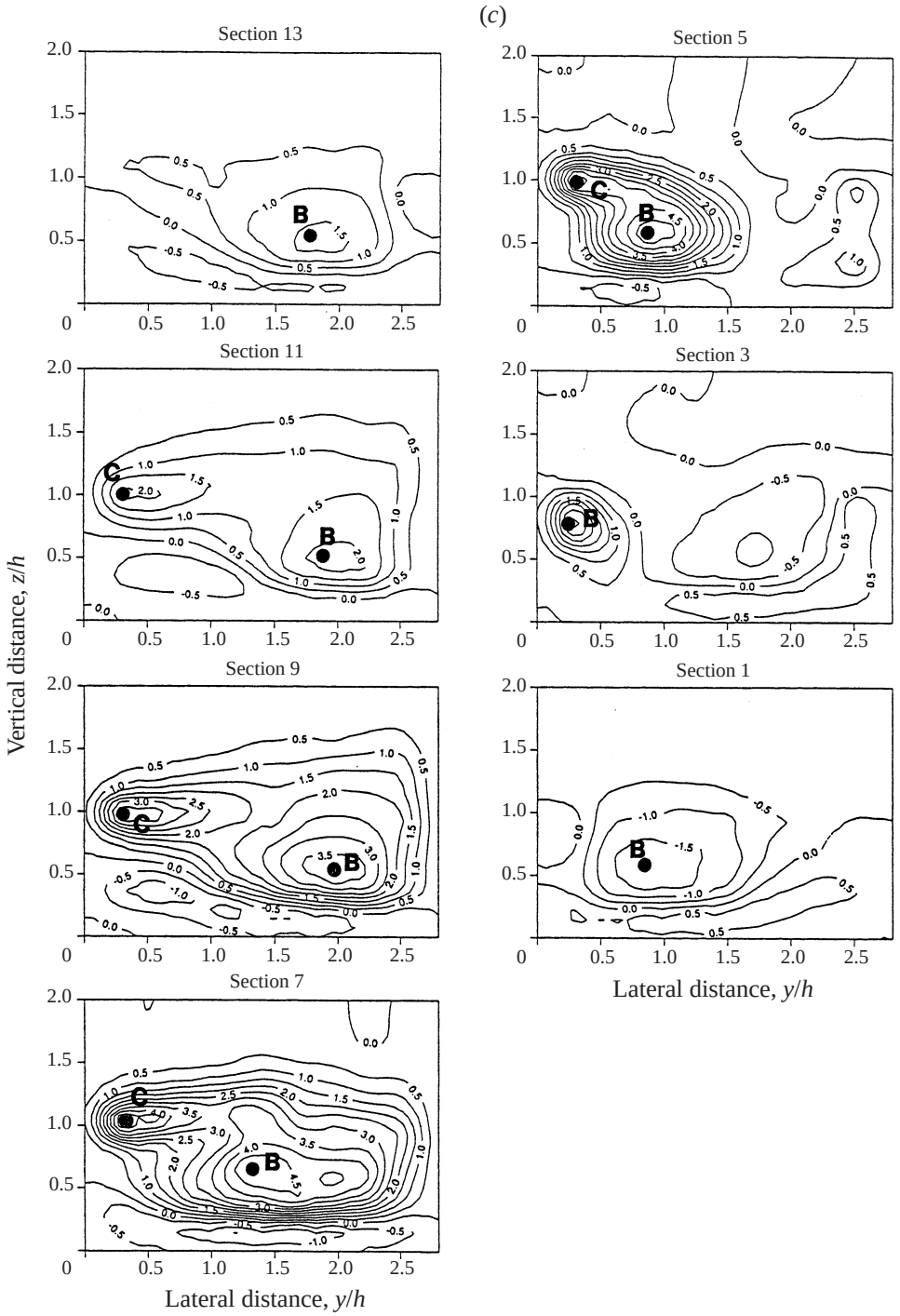

FIGURE 9. Normalized vorticity, $\omega_1 H/U_s$ for $s = 1.37$, (*a*) bankfull, (*b*) $Dr = 0.15$ and (*c*) $Dr = 0.5$.

Term II is the generation of vorticity owing to the stretching and contraction of vortex lines owing to the mean velocity gradients. The stretching of the vortex lines increases the vorticity and contracting decreases it. Along the vortex line, this term can be written by:

$$2\omega_k \omega_j \frac{\partial \overline{U_k}}{\partial x_j} = 2\omega^2 \frac{\partial \overline{U_s}}{\partial s}. \tag{3}$$

U_s is the component of velocity parallel to the vortex line (s direction). Since ω^2 is always positive, the factor $\partial \overline{U_s}/\partial s$ is the rate at which the vortex line is stretching when $\partial \overline{U_s}/\partial s > 0$, or contracting when $\partial \overline{U_s}/\partial s < 0$.

Term III is a reduction rate of vorticity owing to viscous effects.

Term IV describes the effects due to turbulence stresses.

It should be noted that when considering a bend region, the coordinate system has to be changed accordingly.

The streamwise vorticity is defined as:

$$\omega_1 = \left(\frac{\partial \overline{W}}{\partial y} - \frac{\partial \bar{V}}{\partial z} \right). \tag{4}$$

The streamwise vorticity is calculated with the mean values of secondary flow $\bar{V}$ and $\overline{W}$ with the Fleming left hand rule. It is noted that the y-axis and V in figure 8 should be the opposite sign when the Fleming left hand rule is applied, as shown in figure 7. In the calculation, the solid boundaries are assigned $\bar{V} = \overline{W} = 0$, and it is assumed that $\partial \bar{V}/\partial z = 0$ and $\overline{W} = 0$ at the free surface. The results for the $s = 1.370$ case are shown in figure 9. In the figures, ω_1 is normalized by U_s/H. The figure clearly show the difference between secondary flow structure for inbank and overbank flows. For example, for the bankfull case, figure 9(a), three-quarters of the area is occupied by positive values at the apex at section 1, which indicates that two clockwise cells exist. On the other hand, figures 9(b) and 9(c) show some negative areas for both of the overbank cases, which correspond to the two anticlockwise cells seen in figure 8(b) and 8(c).

In addition, the originating mechanisms of secondary flow can be clarified by tracing the growth and decay processes of the dominant cell. These processes can be detected by examining the size and strength of the vorticity identified in the vorticity figures. For example, for the bankfull flow, it can be seen from figure 9(a) that the magnitude of the positive vorticity core generated by the centrifugal force (see A marked in figure 9(a), increases along the bend, which corresponds well with an increase in $\bar{U}$, as can be seen in figure 5(a). This suggests that the $\overline{U_s}$ value ($\sim \bar{U}$ since $\bar{U}$ is the dominant magnitude) increases along the vortex line, i.e. $\partial \overline{U_s}/\partial s > 0$, and ω^2 is always positive and hence the vorticity generation term $\omega^2 \partial \overline{U_s}/\partial s$ becomes positive, implying an increase in clockwise vorticity stretching by the centrifugal force along the bend. This cell therefore develops through a bend section and, thus, has its origin around the entrance to the bend. It can also be seen that this vorticity reduces in strength after leaving the bend, because there is no longer any effect of the centrifugal force in the cross-over reach. The vorticity in the upper-left-hand corner remains and starts increasing in strength after section 9, which corresponds well with an increase in $\bar{U}$. This vorticity prevents the growth of secondary flow owing to the centrifugal force in the whole cross-section along the bend. Judging from this result, it is apparent that the mechanism which governs the secondary flow structure for the inbank case is the centrifugal force and, consequently, the channel geometry of the bend.

For the overbank flows, figure 9(c) shows that for $Dr = 0.5$ there are maximum

positive values of ω_1 along the meandering channel, for example at $y/h \sim 0.25$ and $z/h \sim 0.8$ in section 3, at $y/h \sim 1.0$ and $z/h \sim 0.5$ in section 5, at $y/h \sim 1.5$ and $z/h \sim 0.5$ in section 7, $y/h \sim 2.0$ and $z/h \sim 0.5$ in section 9 and $y/h \sim 1.0$ and $z/h \sim 2.0$ in section 11 (see B marked in figure 9*c*). It may also be noticed that the magnitude of the vorticity core increases along the bend, which corresponds well with an increase in $\overline{U_s}$ ($\sim \bar{U}$), as seen from the magnitude of the streamwise velocity core in figure 5(*c*). This suggests that the vortex is being stretched along the bend since $\omega^2 \partial \overline{U_s}/\partial s > 0$. This vortex stays in the main channel and starts weakening after section 7 in the cross-over region, which also corresponds well with a decrease in the velocity $\overline{U_s}$ ($\sim \bar{U}$). This suggests that the vortex contracts over the latter half of the cross-over region.

At the inner edge along the cross-over region, there are also other large values of ω_1, for example at $y/h \sim 0.4$ and $z/h \sim 1.0$ section 5, $y/h \sim 0.4$ and $z/h \sim 1.0$ section 7, $y/h \sim 0.4$ and $z/h \sim 1.0$ section 9 and $y/h \sim 0.4$ and $z/h \sim 1.0$ section 11 (see C marked in figure 9*c*). They are near the inner edge of the channel and almost at the same locations. This suggests that there are two secondary flow cells, with the same direction of rotation, in the cross-section. Knight & Shiono (1996) show three secondary flow cells with the same direction of rotation at an apex section of a meandering channel with an aspect ratio of 10 for overbank flow. These cells appear to be quite similar in manner to these in this new data. The appearance of an additional cell seems to be related to the large aspect ratio of the FCF channel. It is of interest that a new cell is not formed as a counterpart to the first cell.

The streamwise vorticity generated at the inner edge of the channel at around section 3 is enhanced, enlarged and transported downstream of the cross-over region while generating the next secondary flow at the inner edge of the cross-over region. The secondary flow structure for the overbank cases is controlled by the magnitude of the flood plain flow and, more basically, by the channel geometry of the cross-over region. Secondary flow cells induced by shearing due to the flood plain flow still remain dominantly in the next bend section and, most importantly, they have an opposite sense of rotation to the cells observed for inbank flows. The effect of the centrifugal force can even be seen in the similar regions observed for inbank flows, that is, these cells weaken and change their shapes as they proceed through a bend. This could be caused by the flat fixed bed, but in a morphological channel, it could be stronger. It is of interest to mention that, from the secondary flow structure, the inner bed in a morphological channel bend suffers from erosion and bed materials driven by the secondary flows are deposited on the outer bed during floods. This is the opposite movement of sediment to that which occurs for inbank flows.

8. Spectral analysis

The mean flow analysis in the previous section shows that strong shear layers exist at the bankfull level and at the middle of the cross-section in the cross-over region. The shear will generate turbulence, and the turbulence characteristics in a meandering channel for overbank flow are now considered in detail. Turbulent motion is regarded as a conglomeration of eddies of various sizes or an aggregation of waves of different wavenumbers. The energy spectrum is the most suitable tool for treating such a motion, since it gives information on the contribution of a wavenumber to the total energy.

The spectrum was calculated using a fast Fourier transform (FFT) technique. The sampling rate for the raw data was 100 Hz. The number of data points was $2^{12} = 4096$. Figure 10 shows spatial distributions of spectra for the streamwise component at the

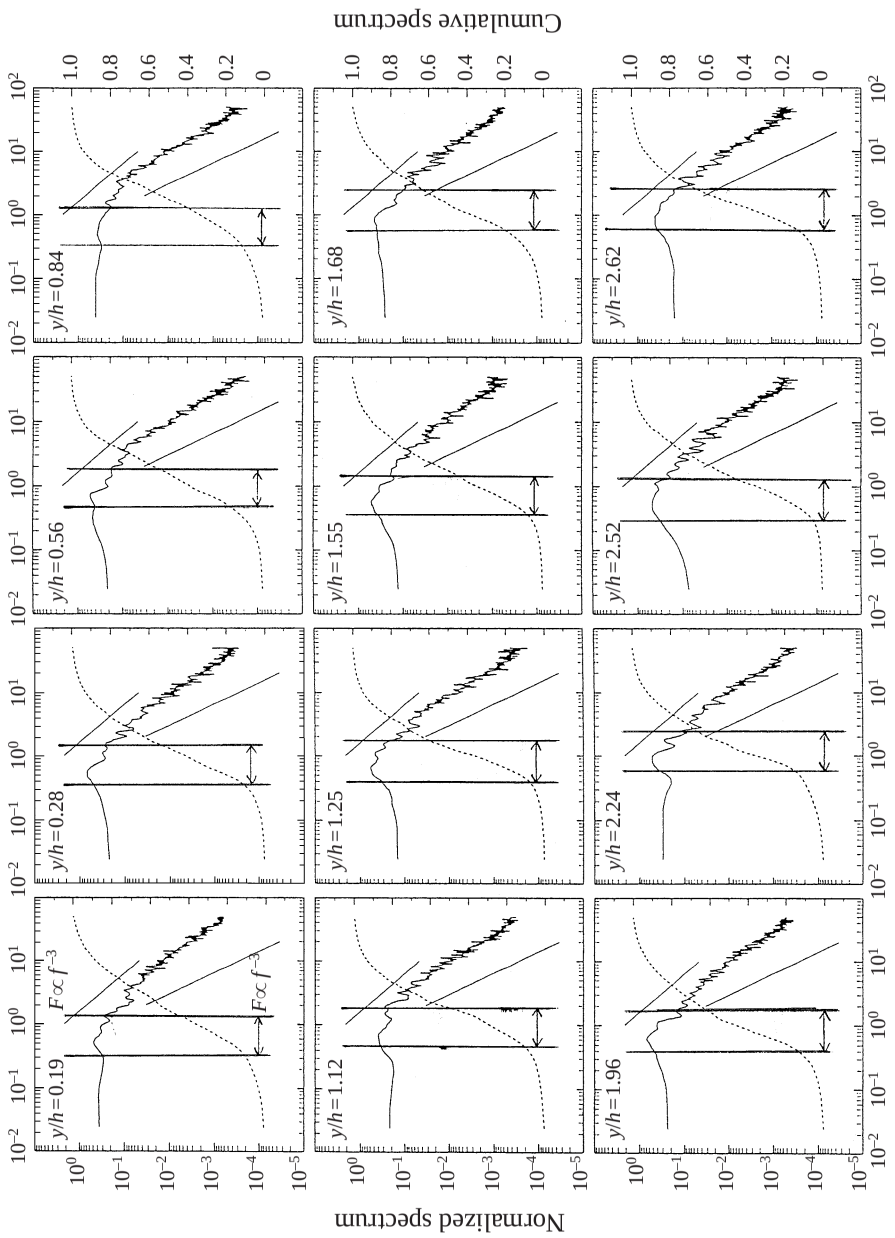

FIGURE 10. Cumulative spectrum at bankfull level in section 7 for $s = 1.37$ and $Dr = 0.5$.

bankfull level in section 7, for $s = 1.370$ and $Dr = 0.50$. Figure 10 also shows the cumulative spectra together with their corresponding frequency spectra. Also indicated in the figures are the gradients of the $-\frac{5}{3}$ power law in the inertial subrange deduced by Kolmogorov and the -3 power law in the viscous subrange by Inoue (1950). Most of the spectra in the figures seem to follow the $-\frac{5}{3}$ power law. This is surprising, first, because of the experimental condition of a small Reynolds number, in which the inertial subrange usually spreads within a narrow range, and secondly because of the strongly three-dimensional nature of the flow, which could severely affect the form of a spectrum, especially in the productive and inertial subranges. On the other hand, it is not clear whether the spectra satisfy the -3 power law in the higher-frequency range.

The figure shows that the positions of spectra which possess a clear peak in their productive subrange are distributed over the whole channel. It is noted from the spectrum distribution shown by Muto (1997) that such spectra mainly appear near the left-hand sidewall in section 5, and toward the right-hand side in section 9. Considering the position of the secondary flow cell in the lower layer shown in figure 8, these peak appearances can be closely related to the secondary flow. The spectral peak appears mainly in the frequency range 0.3 Hz to 1.0 Hz. If Taylor's frozen turbulence hypothesis can be applied, the corresponding lengthscale (the reciprocal of wave-number) is from 2 cm to 8 cm, which is about the order of the main channel depth. The lengthscale which corresponded to the peak frequency was considered as the mean size of the secondary flow cell. Naturally, the size of the secondary flow cell is variable in both space and time, thus such a variation will be reflected in the energy spectrum as a distribution around the peak. In other words, the width of the secondary flow range will be correlated to the variation of the cell size. According to Imamoto, Ishigaki and Nishida (1989), from their cross-sectional flow visualization results, the diameter of the cell generally distributes around its mean d_m from $0.4d_m$ to $1.6d_m$. If this distribution can also be applied to the case considered, the frequency range governed by the secondary flow scale can be estimated as $0.625f_p$ to $2.5f_p$, where f_p is the peak frequency. It can also be considered that the effect of secondary flow is one of the major components of energy expenditure in compound meander flow. The contribution of this effect to turbulent kinetic energy production can be estimated using the cumulative spectrum. To see the contribution of the spectral distribution to the total energy, the cumulative spectrum is considered. The cumulative spectrum $K(f)$ is defined for the streamwise component, for example, as follows:

$$K_u(f) = \frac{1}{u'^2}\int_0^f F_u(f')\,\mathrm{d}f', \tag{5}$$

where $F_u(f)$ = spectrum for u – component, and f = frequency.

For the above range, the estimated contribution to energy production owing to the effect of secondary flow is 35% to 50% for the streamwise component. On the other hand, the turbulence contribution is mostly over 50%. It can be said from this result that the effect of secondary flow on energy production is quite large and it produces as much energy as turbulence does.

9. Turbulence

From the mean flow analysis, it is clear that there are strong interfacial shear and vorticity zones at around the bankfull level and the mid-depth in the cross-over region. This implies that turbulence production exists, owing to the shear produced by the flood plain flow crossing over the main channel flow. The generation mechanisms of

the turbulence can be seen through the turbulence kinetic energy equation. The turbulence kinetic energy equation can be expressed in tensorial notation as

$$\underset{\text{I}}{\frac{\partial \overline{q^2}}{\partial t}+\overline{U_j}\frac{\partial \overline{q^2}}{\partial x_j}}=\underset{\text{II}}{-\overline{u_i u_j}\frac{\partial \overline{U_i}}{\partial x_j}}\underset{\text{III}}{-\frac{\partial}{\partial x_i}\overline{u_i\left(\frac{p}{\rho}+\frac{q^2}{2}\right)}}\underset{\text{IV}}{+\nu\frac{\partial}{\partial x_i}\overline{u_i\left(\frac{\partial u_i}{\partial x_j}+\frac{\partial u_j}{\partial x_i}\right)}}\underset{v}{-\nu\overline{\left(\frac{\partial u_i}{\partial x_j}+\frac{\partial u_j}{\partial x_i}\right)\frac{\partial u_j}{\partial x_i}}}. \quad (6)$$

Term I is the local rate of change of kinetic energy for mean flow and the convective effect of the mean flow on the kinetic energy of the mean flow.

Term II ($-\overline{u_i u_j}\partial\overline{U_i}/\partial x_j$) is the sum of nine terms and is an important group representing the transfer of energy from the mean flow to the turbulence.

Term III is the average work done on an element of fluid by the pressure fluctuation and velocity fluctuations.

Terms IV and V are the work done on an element of fluid by the viscous stresses of the mean flow and the dissipation of energy to heat, respectively.

According to term II in the equation, turbulence is produced only if there are non-zero gradients of mean velocity. From the previous mean flow analysis, there are non-zero gradients of velocity at around bankfull level in the cross-over region in particular. An investigation of the order of magnitude of term II in equation (6) using the measured data in the cross-over section should therefore give insight into turbulence production mechanisms. The magnitudes of the measured normal (as a turbulent intensity) and shear stresses along the meandering channel, are shown first in the following section.

10. Turbulence intensity

Turbulence intensity was obtained for all components as the standard deviation of the temporal velocity variation:

$$u'^2=\frac{1}{T}\sum\{U(t)-\bar{U}\}^2\Delta t. \quad (7)$$

The three intensities, u', v' and w' for the overbank flows correspond well with each other. The values of v' and w' are used for an estimation of the production of the turbulent kinetic energy. The distributions of v' and w' for $Dr = 0.5$ and $s = 1.37$ are shown in figures 11 and 12. The distributions for all the tested depths and configurations can be seen in Muto (1997). In this figure, turbulence intensities are normalized with respect to the friction velocity $u_* = (gRS)^{1/2}$, where R is the hydraulic radius defined at the bend apex and S is the effective energy slope. The effective slope used here is the channel slope for the inbank flow, and the valley slope for the overbank flows, i.e. S_o/s and S_o, respectively. The calculated u_* for each experimental case is listed in table 2.

Figures 11 and 12 show that the highly turbulent intensity areas for both v' and w' along the meandering channel are at roughly similar locations and are near the bed at section 1, around $y/h = 0.5$ and $z/h = 0.9$ in section 3, near the inner edge of the channel and $y/h = 1.0$ and $z/h = 0.6$ in section 5, at $y/h = 1.6$ and $z/h = 0.75$ in section 7, at $y/h = 2.0$ and $z/h = 0.8$ in section 9 and at $y/h = 2.0$ and $z/h = 0.75$ in section 11. From the secondary flow and vorticity figures (figures 8(*c*) and 9), these locations seem to be very close to the centres of the maximum vorticities and the flow intruding from the flood plain. The areas in which the magnitude of normalized turbulence intensities are relatively high, over $2.0u_*$, develop in the upper half-layer of the cross-

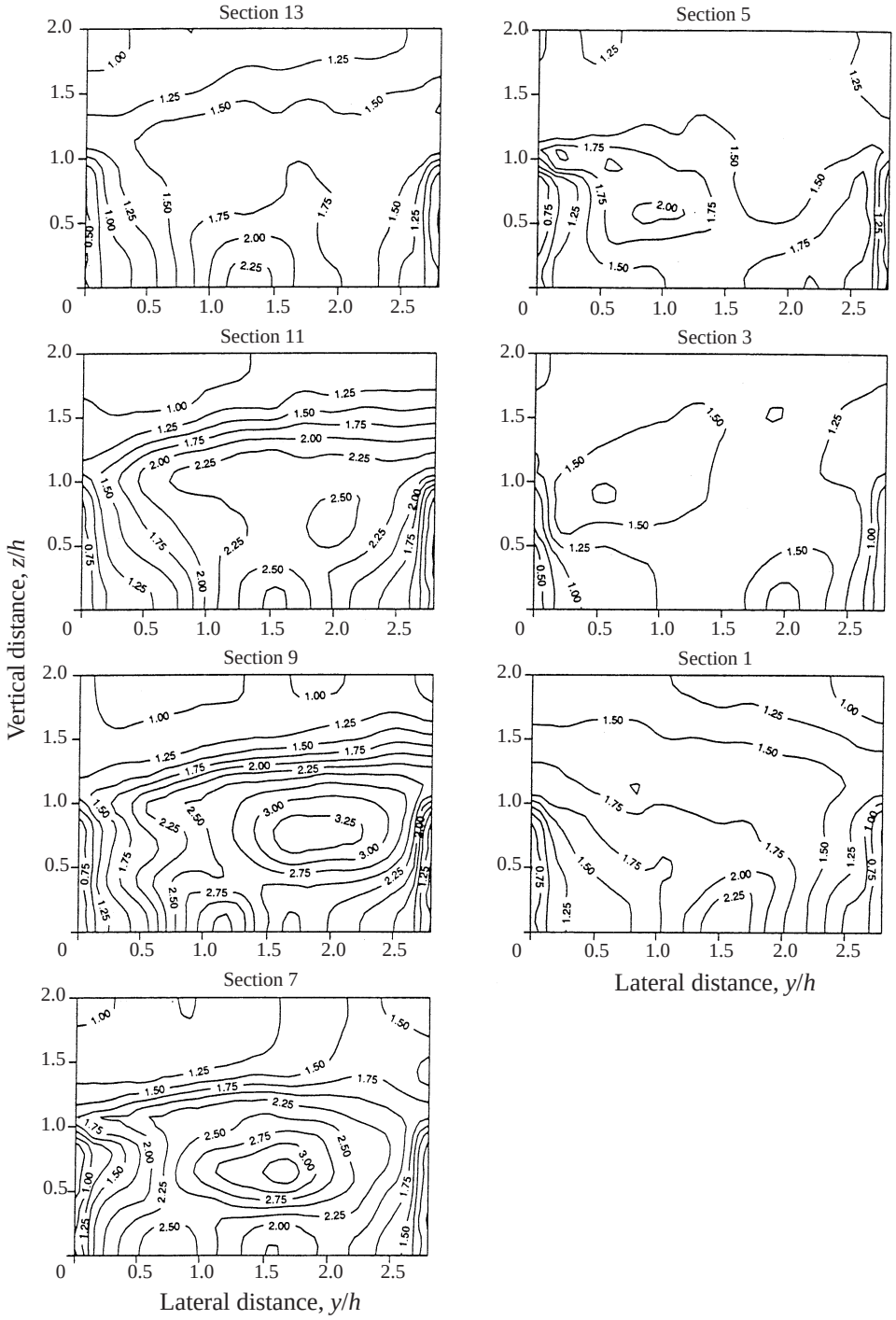

FIGURE 11. Turbulent intensity distributions, v'/u_*, for $Dr = 0.5$ and $s = 1.37$.

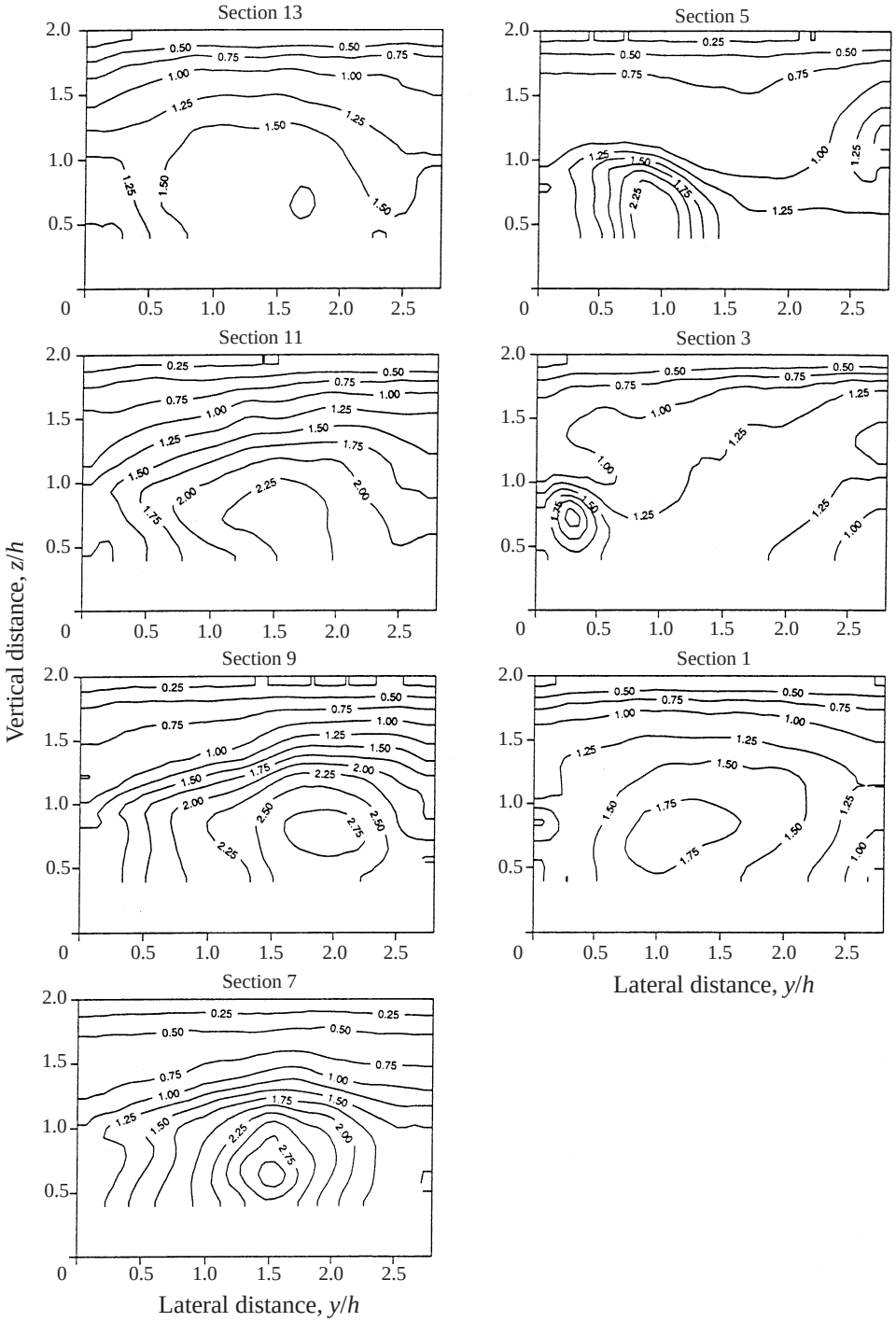

FIGURE 12. Turbulent intensity distributions, w'/u_*, for $Dr = 0.5$ and $s = 1.37$.

	Depth condition Dr	Discharge Q ($\times 10^{-3}$ m^3 s^{-1})	Water depth H (m)	Relative depth H/h	Relative depth $(H-h)/H$	Mean velocity U_s (m s^{-1})	Friction velocity[a] u_* (m s^{-1})	Reynolds number[b] Re ($\times 10^4$)	Froude number[c] Fr
R1	Bankfull	1.876	0.0525	0.980	—	0.237	0.0166	2.63	0.431
	0.15	3.102	0.0633	—	0.154	0.157	0.0121	0.82	0.412
	0.50	25.755	0.1078	—	0.503	0.352	0.0225	6.26	0.495
R2	Bankfull	1.556	0.0519	0.969	—	0.197	0.0148	2.19	0.359
	0.15	2.513	0.0630	—	0.150	0.129	0.0120	0.66	0.340
	0.50	19.996	0.1059	—	0.495	0.282	0.0221	4.92	0.401
R3	Bankfull	1.382	0.0532	0.991	—	0.170	0.0140	1.95	0.307
	0.15	2.204	0.0631	—	0.149	0.113	0.0120	0.62	0.299
	0.50	19.881	0.1087	—	0.506	0.268	0.0226	5.16	0.374

[a] $u_* = (gRS)^{1/2}$, where g = acceleration, due to gravity, R = hydraulic radius and S = energy slope.
[b] $Re = 4U_s R/\nu$, where ν = kinematic viscosity.
[c] $Fr = U_s/(gR)^{1/2}$.

TABLE 2. Hydraulic conditions

sectional area below the bankfull level in the cross-over region. The maximum magnitude of the intensities in the cross-over region is greater than a value of $2.0u_*$ near the bed in a two-dimensional flow case (Nezu & Rodi 1986). The magnitude of w' is generally smaller than the other. It can be seen from the contour lines in the figure that the lower layer is more turbulent than the upper layer. This is most clearly seen in the cross-over sections. The area where the magnitude of turbulence intensities are over $2.0u_*$ extends into the upper layer but remains for $z/h < 1.2$. For inbank flow, the bed- and wall-generated turbulence are generally dominant, but for overbank flows the turbulent intensities just below the bankfull level are the most dominant. The plunging flood plain flow into the main channel induces a large lateral component of the turbulent intensity in the cross-over region.

11. Reynolds stresses

Reynolds stresses are expressed as the temporally averaged product of two components of the velocity variations. That is, if the relevant quantities are treated separately in their mean and variant parts, i.e. $U(t) = \bar{U} + u(t)$ and $W(t) = \bar{W} + w(t)$, the Reynolds stress is expressed as:

$$-\overline{uw} = \frac{1}{T}\sum u(t)\, w(t)\, \Delta t. \tag{8}$$

In the presentation of the results, these stress components are normalized by u_*^2 as defined in the foregoing sections.

Figure 13 shows the measurement results for $-\overline{uw}$. The distribution of $-\overline{uw}$ in $0 < z/h < 0.393$ is presented using the bed shear stress data obtained by a Preston tube, as results being interpolated between these two layers.

In the bankfull flow, figure 13(*a*), the 0-contour line for $-\overline{uw}$ is drawn at around the half-depth level, $z/h = 0.5$, throughout the meander. The lower part below the line shows a monotonic increase of $-\overline{uw}$ towards the channel bed from 0 to $0.6 \sim 1.0u_*^2$, which corresponds to $\partial\bar{U}/\partial z > 0$ in this part (see figure 4). For two-dimensional simple channel cases, the bed shear stress should be equal to $1.0u_*^2$. For these data, it is clear that it is uniformly distributed over the channel width in the cross-over sections, but not so in the bend sections. A higher shearing area is located on the inner side of the channel bend, which corresponds with the location of the core of the primary velocity. In the upper part, $-\overline{uw}$ has negative values, their appearance corresponding well with the behaviour of negative $\partial\bar{U}/\partial z$ (see figure 4) which is induced by the anti-clockwise secondary flow. Their magnitudes are smaller than the bed shear stress values. The maximum value of $|-\overline{uw}|$ in the area can reach $1.0u_*^2$ (section 5), but mostly $0.4 \sim 0.6u_*$.

In the $Dr = 0.15$ flow, figure 13(*b*), the most distinctive region is observed at around the bankfull level in the cross-over, where $-\overline{uw}$ has a negative peak. The region expands its area of dominance through the cross-over and indicates mixing due to the intruding flow from the flood plain as illustrated by Willetts & Hardwick (1993). It first spreads only laterally (sections 3–5) and then also vertically (sections 7–9). These phenomena correspond well to fluid motion like eddy trains observed by the flow visualization and reported by Utami & Ueno (1991). The peaks within the region can appear at the bankfull level and also in the lower layer, $z/h = 0.5$–0.6. The negative peak of $-\overline{uw}$ is about $-1.2u_*^2$ at the cross-over end section (section 9). This is induced by the negative velocity gradient of the main channel velocity at the bankfull level owing to a slower streamwise component of the flood plain flow as illustrated in figure

7. The interaction caused by this velocity difference is therefore one of the most important flow mechanisms for the retardation of the main channel flow. It can also be noticed that, compared with the bankfull flow, the 0-contour line is strongly shifted towards the channel bed in the cross-over sections. This leads to low bed shear stresses in this region, as illustrated by Knight, Yuan & Fares (1992) for a large-scale meander channel investigated in the FCF. The other feature of note is the existence of a positive peak in bend sections. At the apex section, it is situated at around the bankfull level in the centre of the channel and has a peak of $\sim 1.0u_*^2$. This indicates that the flow in the main channel below the bankfull level at the bend apex is slower than that in the upper layer, hence the momentum transfer occurs from the upper layer to the lower layer. It can be deduced from the shear stress behaviour at the cross-over section and the apex section that the loss or gain of the momentum in the main channel is dependent on the magnitude of the streamwise component of the flood plain flow. This means that the angle of the flood plain flow entering into the meander channel is an important parameter governing the main channel flow.

The $Dr = 0.50$ flow, figure 13(*c*), basically shows similar features to the $Dr = 0.15$ flow for the distribution of $-\overline{uw}$. The peak value in the negative region is $-2.0u_*^2$ and that in the positive region is about $1.0u_*^2$. It should be noted that the position of the core of the positive region can be located at $z/h > 1.0$, slightly above the bankfull level. This is due to an increase in the streamwise component of the flood plain flow as the water depth increases (see figure 7). Water depth is also another important parameter influencing the main flow.

From the above observations for $-\overline{uw}$ for the overbank flows, it can be seen that the turbulent shear generated at around the bankfull level is more dominant than the bed generated turbulence, and such shear strongly affects the flow structure. The appearances of negative and positive values of $-\overline{uw}$ in the shearing region indicate that the lower-layer flow is accelerated in the streamwise direction by the upper-layer one in bends, whereas it is decelerated in the cross-over, and vice versa.

The cross-sectional distribution of $-\overline{vw}$ is shown in figure 14. The results indicate the existence of strong vertical shearing in the lateral direction at around the bankfull level in the cross-over region. An area of relatively large positive $-\overline{vw}$ value is seen to develop in a similar manner to the negative $-\overline{uw}$ area. This again suggests that the flow intrusion from the flood plain into the main channel, and the result interaction between the upper and lower flows, strongly affect the flow structure in compound meander channels during floods. The maximum of $-\overline{vw}$ can reach $2.5u_*^2$ in the $Dr = 0.15$ case and $4.0u_*^2$ in the $Dr = 0.50$ case. The appearance of the core of the area is slightly below the bankfull level, $z/h = 0.6$–0.8, for the $Dr = 0.50$ case and its location coincides with the centre of secondary flow. It can be said that this vigorous shear $-\overline{vw}$ in the cross-over regions is induced by the strong secondary flows observed in the lower layer for the overbank flow cases.

12. Turbulence energy production

The Reynolds stress $-\overline{vw}$ component was measured only over the cross-over region, therefore an analysis of the turbulence kinetic energy production could be carried out for this region. Since the cross-over region is a straight reach, a Cartesian coordinate system can be assumed and an expansion of the term II in equations (6) gives

$$\text{Prod} = -u'^2\frac{\partial \bar{U}}{\partial x} - v'^2\frac{\partial \bar{V}}{\partial y} - w'^2\frac{\partial \bar{W}}{\partial z} - \overline{uv}\left(\frac{\partial \bar{U}}{\partial y} + \frac{\partial \bar{V}}{\partial x}\right) - \overline{uw}\left(\frac{\partial \bar{U}}{\partial z} + \frac{\partial \bar{W}}{\partial x}\right) - \overline{vw}\left(\frac{\partial \bar{V}}{\partial z} + \frac{\partial \bar{W}}{\partial y}\right). \quad (9)$$

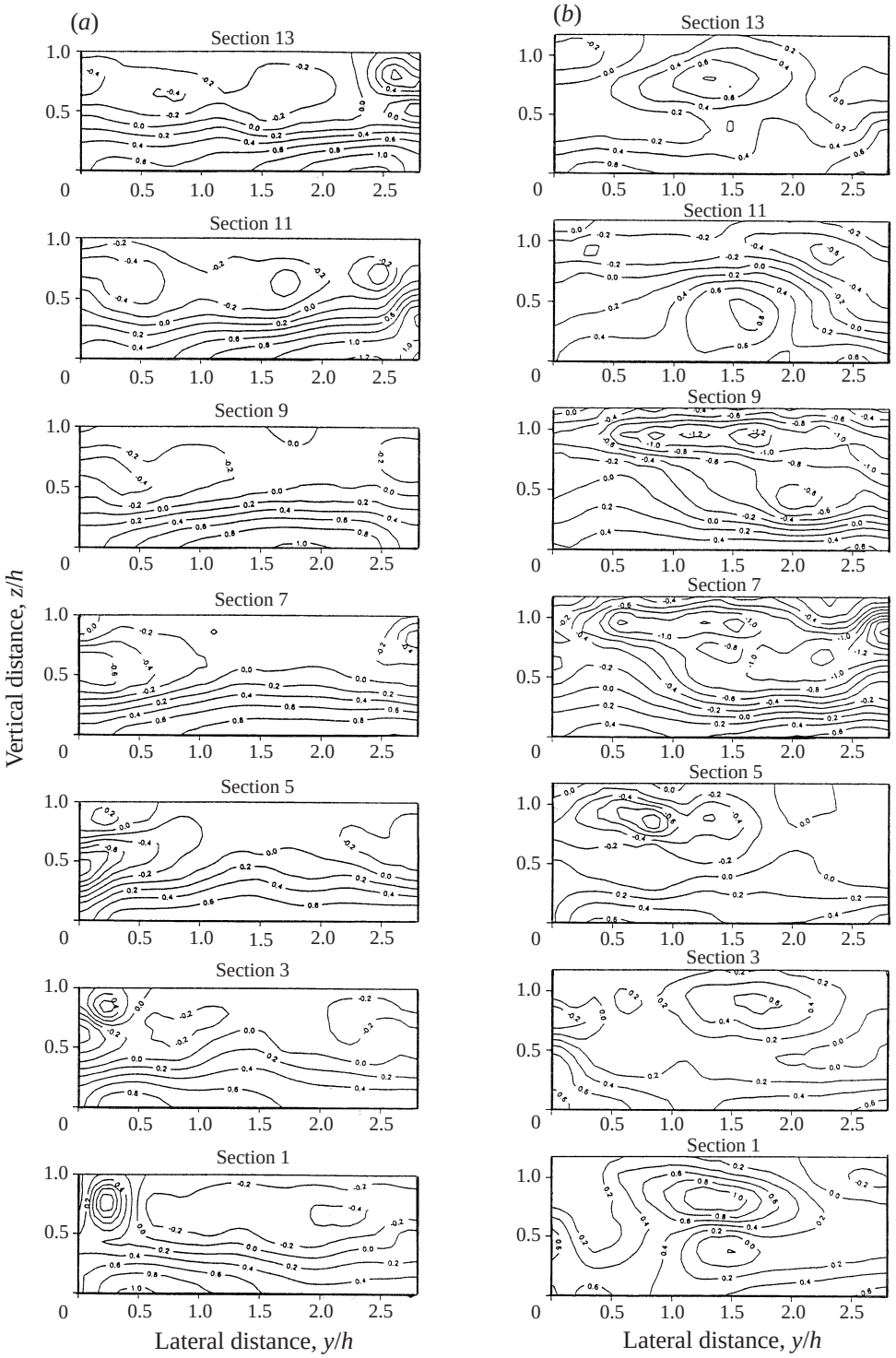

FIGURE 13(*a*, *b*). For caption see facing page.

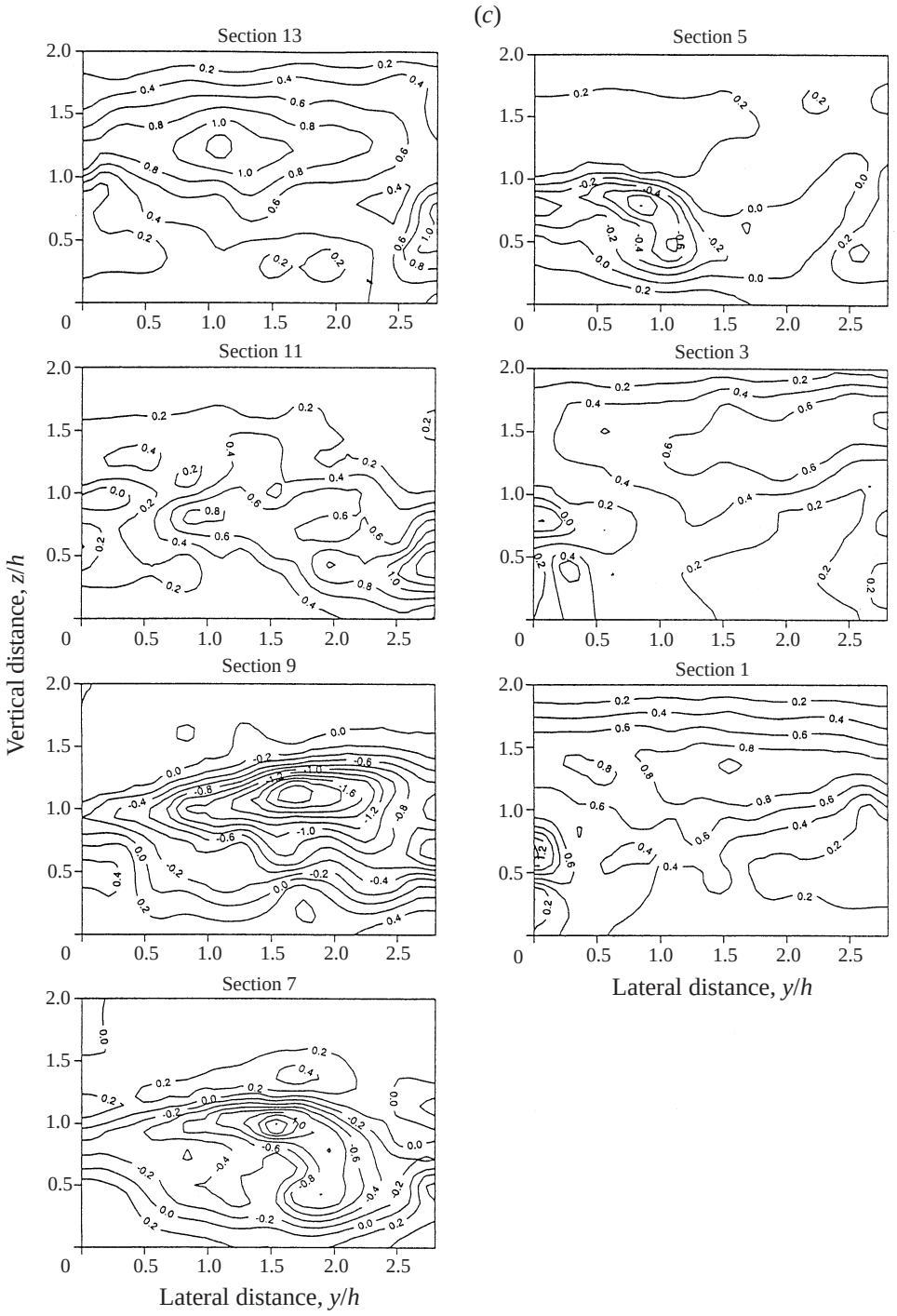

FIGURE 13. Reynolds stress distributions $-\overline{uw}/u_*^2$ for $s = 1.37$, (*a*) bankfull, (*b*) $Dr = 0.15$ and (*c*) $Dr = 0.5$.

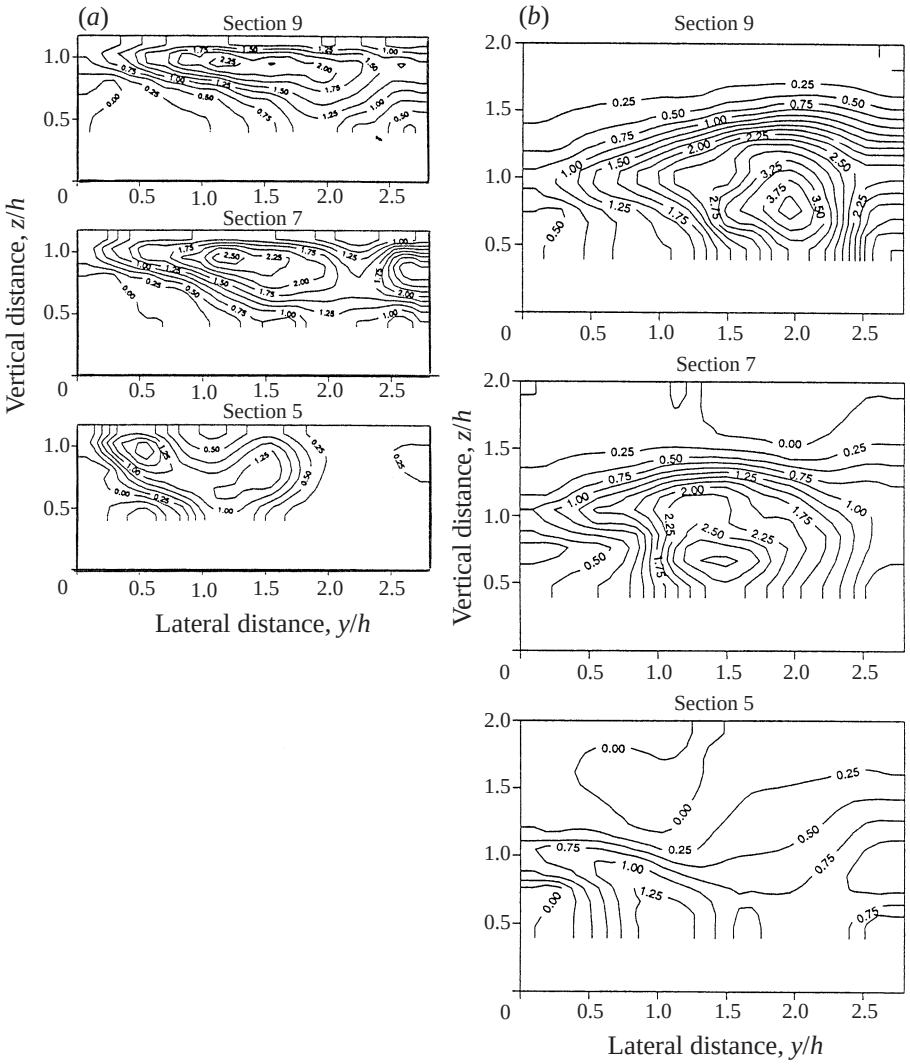

FIGURE 14. Reynolds stress distributions, $-\overline{vw}/u_*^2$, for $s = 1.37$, (*a*) $Dr = 0.15$ and (*b*) $Dr = 0.5$.

Clearly, u'^2 is positive and the first set will have the effect of transferring energy from the mean flow to the turbulence if $\partial\bar{U}/\partial x$ is negative and conversely if it is positive. The remaining correlations ($i \neq j$) are expected to be negative if the shearing strains are positive. As far as the mean flow is concerned, these terms are dissipative, in the sense that the flow of energy is from the mean flow to the turbulence and does not reverse.

The derivatives in terms of the x-direction (streamwise direction) is one order of magnitude smaller than those of the other directions, so the above equation can be reduced to

$$\text{Prod} = -v'^2\frac{\partial\bar{V}}{\partial y} - w'^2\frac{\partial\bar{W}}{\partial z} - \overline{uv}\left(\frac{\partial\bar{U}}{\partial y}\right) - \overline{uw}\left(\frac{\partial\bar{U}}{\partial z}\right) - \overline{vw}\left(\frac{\partial\bar{V}}{\partial z} + \frac{\partial\bar{W}}{\partial y}\right). \tag{10}$$

The energy production, normalized by u_*^3/H, due to the last three terms of the shear stresses in equation (10), was first calculated and is shown in figure 15. It can be seen

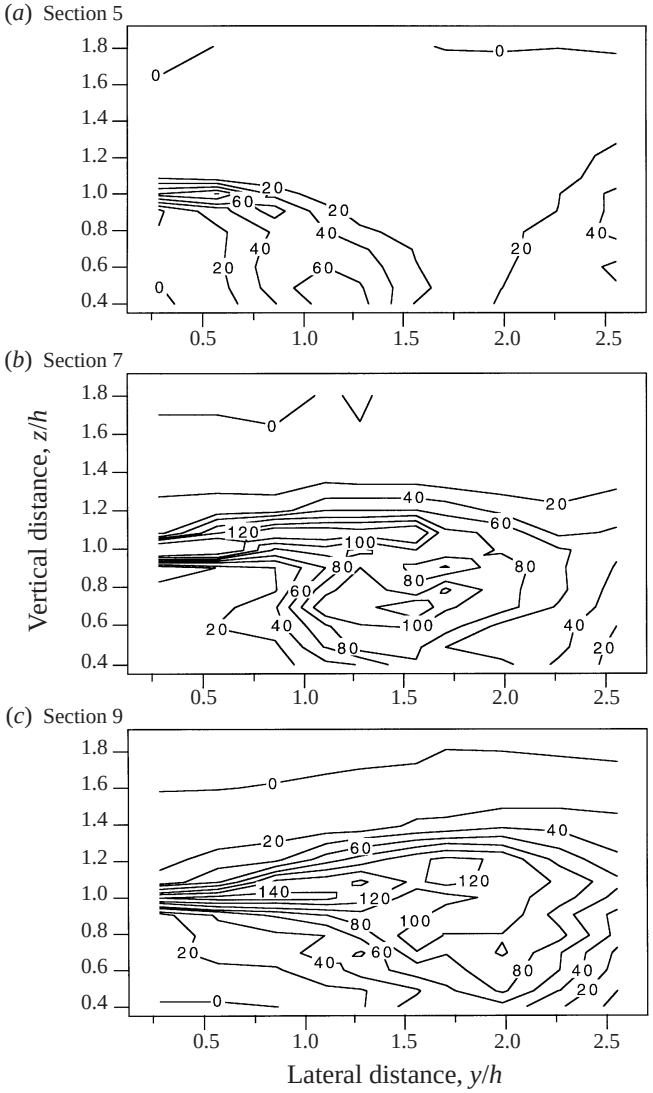

FIGURE 15. Turbulent kinetic energy production distributions, $\mathrm{Prod}/(u_*^3/H)$ due to shear stresses in cross-over region for $s = 1.37$ and $Dr = 0.5$.

from the figure that, in section 5, there are two peaks near the inner edge of the channel at the bankfull level and at $y/h = 1.2$ and $z/h = 0.4$. These locations agree well with those in which large magnitudes of the vorticity appear owing to shearing by the flood plain flow crossing over the main channel at the inner edge of the channel and owing to the flood plain flow plunging into the main channel. From figures 5, 8, 13 and 14, the shear stress, $-\overline{vw}$, value in the core region is 3–4 times the $-\overline{uw}$ value and $(\partial\bar{V}/\partial z)+(\partial\overline{W}/\partial y)$ is larger than $\partial\bar{U}/\partial z$, hence the main contribution of the shear production in the strong secondary flow region comes from the $-\overline{vw}$ term generated by the secondary flows. In contrast, $-\overline{uw}(\partial\bar{U}/\partial z)$ and $-\overline{uv}(\partial\bar{U}/\partial y)$ are main contributors to the turbulence energy production in secondary flow regions for straight compound channels, as reported by Tominaga & Nezu (1991). A similar trend can be seen in sections 7 and 9. The shear production of the turbulent kinetic energy is of the

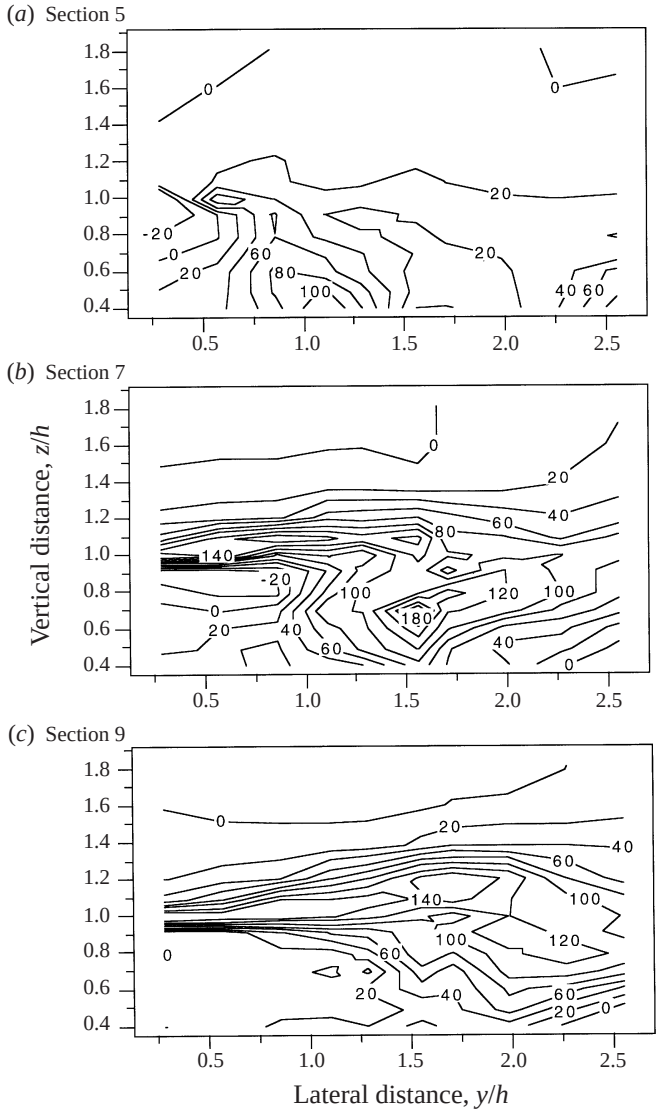

FIGURE 16. Turbulent kinetic energy production distributions, $\mathrm{Prod}/(u_*^3/H)$ in cross-over region for $s = 1.37$ and $Dr = 0.5$.

order of 100 and significantly larger than that produced by transverse shearing in a straight compound channel for overbank flow (Tominaga & Nezu 1991).

The full terms of equation (10) were also calculated and are shown in figure 16. The figure shows that most turbulence production (Prod > 0) occurs at similar locations to the shear production, but the magnitudes in the core regions are increased to about twice that previously. The normal stress terms thus contribute to the energy production as much as the shear stress terms do. This is mainly caused by the deceleration of $\bar{V}$ in the y-direction and $\bar{W}$ in the z-direction owing to the flood plain flow mixing with the main channel flow while the flood plain flow is crossing over the main channel, as seen in previous sections (i.e. $-v'^2\partial\bar{V}/\partial y$) with $\partial\bar{V}/\partial y < 0$ and $-w^2(\partial\bar{W}/\partial z) > 0$ with $(\partial\bar{W}/\partial z < 0)$.

It is of interest to observe that there exist some areas which have negative values, for example, at around the bankfull level near the edge of the channel in section 5 and below the bankfull level in the inner region of the channel in section 7. In these regions, as soon as the flood plain flow enters the main channel, the flood plain flow streamline dips down sharply as a result of the pressure difference induced by the slower flood plain flow near flood plain bed (higher pressure) entering the faster main channel flow (lower pressure) and gradually recovers this dip by reducing the pressure difference owing to the fluid mixing by the turbulence along the cross-section. This creates $\partial \bar{V}/\partial y > 0$ and hence $-v'^2(\partial \bar{V}/\partial y) < 0$. The negative production means that the normal stress terms withdraw the turbulence energy more than the production owing to the shear in those regions.

The major production of turbulent kinetic energy due to the shear stresses is clearly seen in the secondary flow area and near the inner edge of the channel. The shear energy production is mainly generated by the shear stress of $-\overline{vw}$ due to the secondary flows. It is of interest that there are no energy production areas, owing to the turbulence production terms, in which the normal stress terms withdraw the energy more than the shear stress term produce it.

13. Eddy viscosity

Eddy viscosity is commonly used to analyse momentum transfer and is often used in numerical models. An investigation of eddy viscosity was carried out in specific areas. The areas chosen were in high shear and strong secondary flow regions in order to see the change of the eddy viscosity magnitude for all the sinuosity cases tested. The strongest shear in the cross-over section amongst the tested cases was $s = 1.57$ ($\theta = 90°$) since the streamwise component of the flood plain flow becomes almost zero, while that for the main channel flow is non-zero. The eddy viscosity, ε, was calculated using a velocity gradient and a maximum shear stress in the strong shear region (e.g. $y/h = 0.56$ in section 7) for $Dr = 0.5$ and $s = 1.57$:

$$-\overline{uw} = \varepsilon\left(\frac{\partial \bar{U}}{\partial z} + \frac{\partial \bar{W}}{\partial x}\right), \tag{11}$$

and was $0.07 \times 10^{-3}\ \mathrm{m^2\ s^{-1}}$, which implies that the non-dimensional eddy viscosity, $\varepsilon/(u_* H)$, was 0.030. It is noted that the non-dimensional eddy viscosity has no physical meaning, but can be used simply as a cross-reference. The shear stresses were reproduced using this constant eddy viscosity, assuming the high shear region to be free turbulence flow (Schlichting 1978), and the measured velocity data. It was assumed that $\partial \bar{W}/\partial x = 0$ in this region because the change of $\bar{W}$ in the streamwise direction in the shear layer can be negligible compared with the change of $\bar{U}$ in the vertical direction. This eddy viscosity reproduces reasonable values for the measured shear stress distributions for different sinuosities as shown by the results in figure 17. However, near the bed region, the reproduced shear stress is not in good agreement with the experimental data, which is understandable because the eddy viscosity in the wall turbulent flow region varies considerably (Nezu & Rodi 1986). In the strong secondary flow region, namely at $y/h = 2.0$, the shear stress was calculated with the same eddy viscosity value and is shown in figure 17(*b*). The maximum shear stress for each sinuosity is about half the measured value. This could be caused by either the eddy viscosity being too small or the assumption of the velocity gradient, $\partial W/\partial x = 0$ being incorrect.

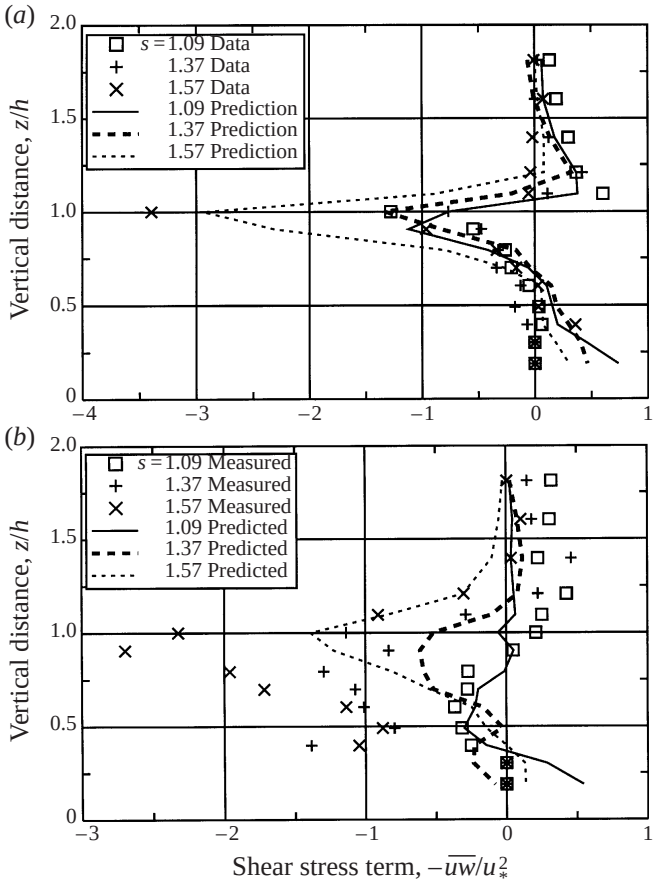

FIGURE 17. Predicted and measured shear stress, $-\overline{uw}/u_*^2$, distributions with different sinuosities. (*a*) Location $y/h = 0.56$ in section 7. (*b*) Location $y/h = 2.0$ in section 7.

This may be clarified using the measured values of $\bar{W}$ and $\bar{V}$. At $y/h = 0.56$ and $y/h = 2.0$ in section 7 for $Dr = 0.5$, both velocity gradients of $\partial\bar{W}/\partial y$ and $\partial\bar{V}/\partial z$ were estimated from the data, and using a maximum value of $-\overline{vw}$ at $y/h = 0.56$, the eddy viscosities become 0.07×10^{-3} m^2 s^{-1} for $s = 1.37$ and 1.57 but 0.1×10^{-3} m^2 s^{-1} for $s = 1.09$. There exists a noticeable secondary flow in this region for $s = 1.09$ (Muto 1997). At $y/h = 2.0$, the eddy viscosities are 0.17×10^{-3} m^2 s^{-1} for $s = 1.37$ and 1.57 and 0.13×10^{-3} m^2 s^{-1} for $s = 1.09$. For $s = 1.09$, weaker secondary flow was observed (Muto 1997). Thus, the magnitude of the eddy viscosity in this region is substantially increased. The shear stress distributions calculated, using the above eddy viscosities, together with the measured shear stress distributions are shown in figure 18. The peak shear stress at each sinuosity is reproduced well.

An investigation into the effect of the velocity gradients on the shear stress was carried out using the following three sets of assumptions: case (i) 0.17×10^{-3} m^2 s^{-1} eddy viscosity and the velocity gradients, $\partial\bar{W}/\partial y$ and $\partial\bar{V}/\partial z$, case (ii) 0.17×10^{-3} m^2 s^{-1} eddy viscosity and only $\partial V/\partial z$ and case (iii) 0.07×10^{-3} m^2 s^{-1} eddy viscosity and $\partial\bar{V}/\partial z$. The shear stress results are shown in figure 19. For cases (i) and (ii) the shear stress is reproduced well for the region below the bankfull level, but not for that above the bankfull level. This indicates that $\partial\bar{V}/\partial z$ is more significant than $\partial\bar{W}/\partial y$. For case (iii) the estimated $-\overline{vw}$ agrees well with that measured above the bankfull level but

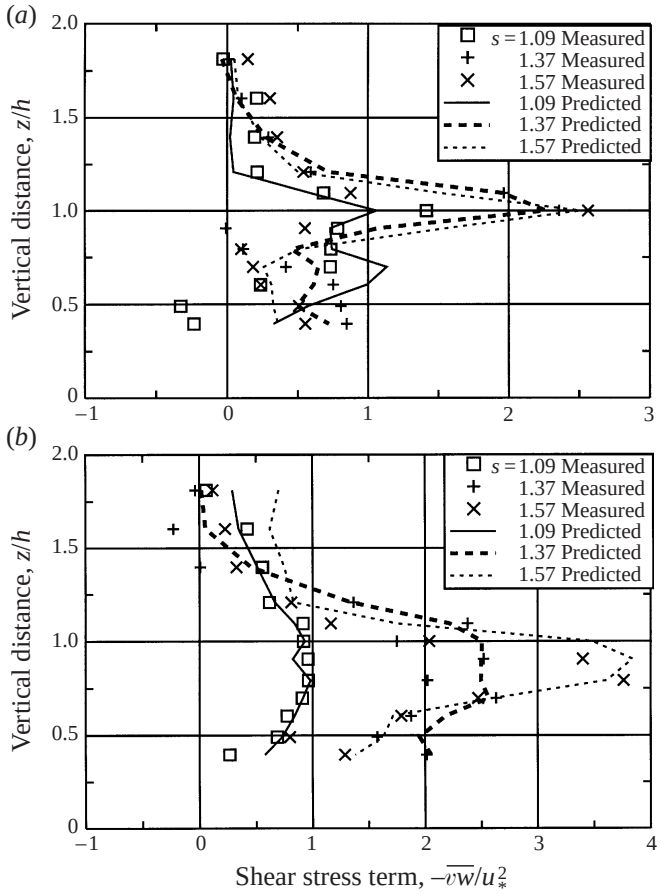

FIGURE 18. Predicted and measured shear stress, $-\overline{vw}/u_*^2$, distributions with different sinuosities. (*a*) Location $y/h = 0.56$ in section 7. (*b*) Location $y/h = 2.0$ in section 7.

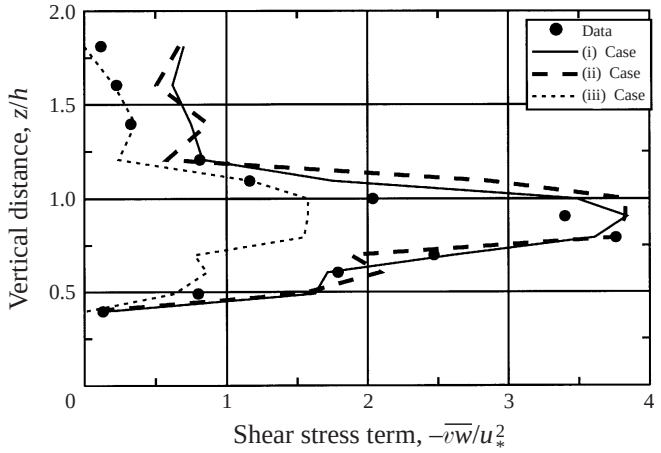

FIGURE 19. Shear stress distributions, $-\overline{vw}/u_*^2$, with three different conditions: (i) 0.17×10^{-3} m^2 s^{-1} eddy viscosity and the velocity gradients, $\partial\bar{W}/\partial y$ and $\partial\bar{V}/\partial z$, case (ii) 0.17×10^{-3} m^2 s^{-1} eddy viscosity and only $\partial\bar{V}/\partial z$ and case (iii) 0.07×10^{-3} m^2 s^{-1} eddy viscosity and $\partial\bar{V}/\partial z$.

there is a substantial reduction in the maximum shear stress. When an eddy viscosity value of 0.17×10^{-3} m^2 s^{-1} (or $\varepsilon/(u^*H) = 0.073$) is used, the maximum shear stress $-\overline{vw}$ is more of less the same as that measured in the strong secondary flow region. On the other hand, when the 0.07 value (or $\varepsilon/(u^*H) = 0.030$) is used, the shear stress in the strong shear region is reproduced well. In unidirectional flows, such as, for example, straight compound channel flows, shear is mainly generated by the streamwise velocity difference in the lateral direction as shown by Shiono & Knight (1991). They show that the non-dimensional depth-averaged eddy viscosity in the main channel is about $\varepsilon/(u^*H) = 0.07$, which is produced by a combination of bed and shear generated turbulence. The value is surprisingly similar to that in the strong secondary flow region. From the analysis of the eddy viscosity carried out above, it can be said that there exist two turbulence flow characteristics within the cross-section in the cross-over region. One is free turbulence flow above the bankfull level at the inner edge of the channel and the other is the combined wall and shear generated turbulence below the bankfull level. Numerical modellers often use the eddy viscosity model and the k–ϵ model for solving flows in open channels, and it is hoped that these eddy viscosity results might be useful for them in validating their results, although the analysis here is obviously limited.

14. Concluding remarks

This paper has looked mainly into the generation mechanisms of secondary flow and turbulence in meandering channels with different sinuosities. Given the fact that turbulence measurements were only obtained at two relative depths ($Dr = 0.15$ and 0.5), it is now possible to begin to define the flow structure in such channels. The dominant secondary-flow generation mechanism is shown in figure 20 together with the main contributions to turbulence energy production in the cross-over region. It should be remembered that the main channel aspect ratio was unnaturally low. Furthermore, factors which were not taken into account, such as the wall roughness (including vegetation on the flood plain), the sinuosity of the flood plain banks and their relative phase to that of the main channel and movable bed materials, should also be considered as determinants. Further research exploring the effects of these factors on the flow structure is currently being undertaken by researchers using the FCF at HR Wallingford UK. However, from the LDA turbulence measurements undertaken in the meander channels tested so far, the following conclusions may be drawn:

(i) When the flow visualization results are compared with the velocity measurements in compound meander channels, they indicate that the flow behaviour on the water surface is closely related to the upper-layer flow structure when the depth of flooding is low, but is not related to the complex internal flow structure when the depth of flooding is high.

(ii) For low flood water depths, significant deflection of the flow in the upper-layer flow is caused by the interaction between the upper- and lower-layer flows, which induces a lateral velocity gradient and hence generates vertical vortices corresponding to an area appearing like an eddy train. When the flood water depth becomes deeper, the interaction is less significant and these two layer flows are less dependent on each other.

(iii) The strong vertical shear layer generated by the flood plain flow crossing over the main channel flow is controlled by the angle between the meandering channel and the flood plain wall and water depth. In contrast, for a straight compound channel the shear is normally generated by the lateral velocity difference between the main channel and flood plain flows. The shearing mechanisms between a straight compound channel

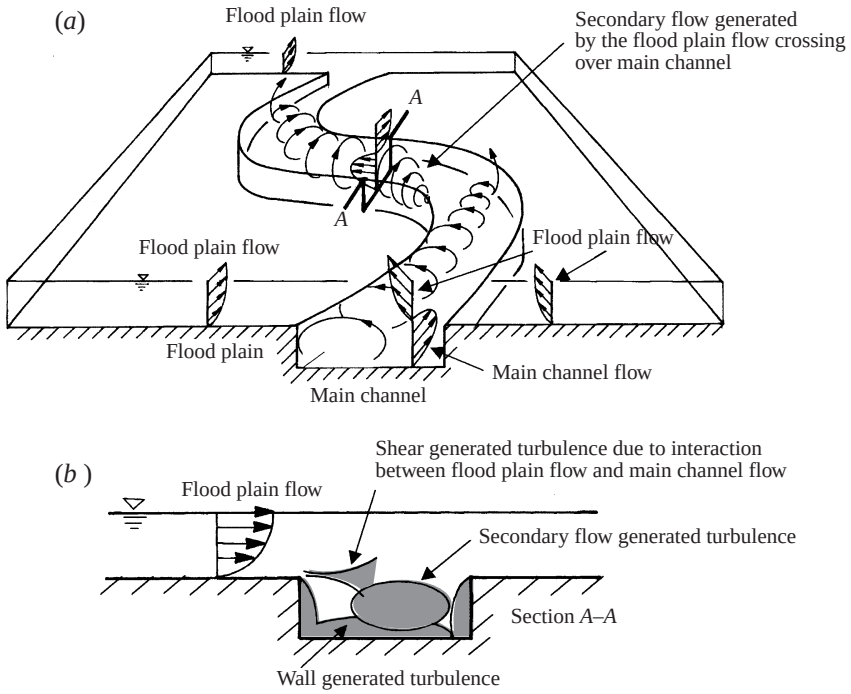

FIGURE 20. Overall flow structure in meandering channel for overbank. (*a*) Secondary flow generation mechanism. (*b*) Main contributions to turbulence energy production in cross-over section.

and a meander compound channel with straight flood plain banks for overbank flow are therefore significantly different.

(iv) The measured secondary flow confirms that the most important feature of secondary flow structures in meandering channels is the opposite sense of rotation of the secondary flow cell at bend apexes before and after inundation, and originating from different mechanism for inbank and overbank flows. For inbank flow, the vorticity analysis shows an increase in clockwise vorticity by stretching owing to the centrifugal force along the bend, and a decrease in size over the cross-over region after leaving the bend for inbank flow. For overbank flow, two clockwise vortices are generated by the flood plain flow crossing over the main channel flow in the cross-over region. These two cells are not formed as a reaction to each other.

(v) The spectral peak appears mainly in the frequency range 0.3 Hz to 1.0 Hz, which corresponds to a lengthscale from 2 cm to 8 cm. This is considered to be caused by the effect of the secondary flow. The effect of secondary flow on energy production was found to be large, producing as much energy as the turbulence does.

(vi) For inbank flow, the bed- and wall-generated turbulence is generally the most dominant feature, but for overbank flows the turbulent intensities just below the bankfull level become more important. This is also supported by observations on $-\overline{uw}$ for overbank flows, which show that the shear generated turbulence at around the bankfull level is more dominant than the bed generated turbulence and strongly affects the flow structure. However, the magnitude of the shear stress $-\overline{vw}$ induced by the strong secondary flows in the lower layer, can reach 3–4 times the bed generated turbulence and the value of $-\overline{uw}$.

(vii) The turbulent kinetic energy production analysis shows that the main contribution of the shear stresses to the turbulence production in the strong secondary

flow region come from the $-\overline{vw}$ term generated by the secondary flows. In contrast, $-\overline{uw}(\partial\bar{U}/\partial z)$ and $-\overline{uv}(\partial\bar{U}/\partial y)$ are main contributors to the turbulence energy production in secondary flow regions for straight compound channels. The negative values of the turbulence production due to the normal stress terms exist near the inner edge of the channel in the cross-over region. The normal stress terms withdraw the turbulence energy rather than produce it.

(viii) The eddy viscosity analysis shows that there are two turbulence flow characteristics which exist within the cross-section in the cross-over region. One is free turbulence flow which occurs above the bankfull level at the inner edge of the channel, and the other is the combined wall and shear generated turbulence below the bankfull level. The eddy viscosity becomes larger when the flow possesses secondary flow. It may also serve as a test case for numerical modelling.

We gratefully acknowledge the financial support of the Engineering and Physical Sciences Research Council (GH/H/14755). We are also grateful to Professor D. W. Knight of the University of Birmingham for his helpful comments during the preparation of this paper. Y. M. would like to thank Dr A. F. L. Hyde in his role as Postgraduate Tutor whilst at Bradford University. We would like to thank Professors H. Imamoto and T. Ishigaki for undertaking the visualization experiments at DPRI, Kyoto University.

REFERENCES

Elliott, S. C. A. & Sellin, R. H. J. 1990 SERC flood channel facility: skewed flow experiments. *J. Hydraul. Res.* **28**, 197–214.

Ervine, D. A. & Ellis, J. 1987 Experimental and computational aspects of overbank floodplain flow. *Trans. R. Soc. Edin. Earth Sciences* **78**, 315–325.

Ervine, D. A., Sellin, R. J. & Willetts, B. B. 1994 Large flow structures in meandering compound channels. *2nd Intl Conf. on River Food Hydraulics*, pp. 459–469. York, UK.

Ervine, D. A., Willetts, B. B., Sellin, R. H. J. & Lorena, M. 1993 Factors affecting conveyance in meandering compound flows. *J. Hydraul. Engng ASCE* **119**, 1383–1399.

Fukuoka, S. & Fujita, K. 1989 Prediction of flow resistance in compound channels and its application to design of river courses. *Proc. JSCE* **411/II-12**, 63–72 (in Japanese).

Imamoto, H., Ishigaki, T. & Fujisawa, H. 1982 On the characteristics of open channel flow in bends with flood plains (1). *Annuals DPRI, Kyoto University* **25B-2**, 529–543 (in Japanese).

Imamoto, H., Ishigaki, T. & Nishida, M. 1989 Experimental study on the turbulent flow in a trapezoidal open channel. *Annuals DPRI, Kyoto University* **32B-2**, 935–949 (in Japanese).

Imamoto, H., Ishigaki, T. & Muto, Y. 1991 On the hydraulics of an open channel flow in complex cross-section. *Annuals DPRI, Kyoto University* **34B-2**, 387–399 (in Japanese).

Imamoto, H. & Kuge, T. 1974 On the basic characteristics of an open channel flow in complex cross section. *Annuals DPRI, Kyoto University* **17B**, 665–679 (in Japanese).

Inoue, E. 1950 The micro scale of turbulence. Research report, University of Tokyo, vol. 4, pp. 194–200 (in Japanese).

Kiely, G. K. 1989 An experimental study of overbank flow in straight and meandering compound channels. PhD thesis, University College, Cork, Ireland.

Knight, D. W. & Shiono, K. 1990 Turbulent measurements in a shear layer region of a compound channel *J. Hydraul. Res.* **28**, 175–196.

Knight, D. W. & Shiono, K. 1996 River channel and floodplain processes. In *Floodplain Processes* (ed. Anderson, Walling & Bates), chap. 5, pp. 139–181. J. Wiley.

Knight, D. W., Yuan, Y. M. & Fares, Y. R. 1992 Boundary shear in meandering channels. *Proc. Intl Symp. on Hydraulics in Natural and Laboratory Conditions*, vol. 2, pp. 102–107. Yantze River Scientific Research Institute, Wuhan, China.

MUTO, Y. 1997 Turbulent flow in two stage meandering channels. PhD thesis, University of Bradford, UK.

NEZU, I. & NAKAGAWA, H. 1993 Turbulence in open-channel flows. IAHR Monograph Series, A. A. Balkema, Rotterdam, Netherlands.

NEZU, I. & RODI, W. 1986 Open-channel flow measurements with a laser Doppler anemometer. *J. Hydraul. Engng ASCE* **112**, 335–355.

ROZOVSKII, I. L. 1961 *Flow of Water in Bends of Open Channels*. Israel Program for Scientific Translation, Jerusalem, Israel (originally in Russian, the Academy of Science of the Ukraine SSR, 1957).

SCHLICHTING, H. 1978 *Boundary Layer Theory*, pp. 729–757. McGraw-Hill.

SELLIN, R. H. J. 1964 A laboratory investigation into the interaction between the flow in the channel of a river and that over its floodplain. *La Houille Blanche*, **7**, 793–802.

SELLIN, R. H. J., ERVINE, D. A. & WILLETTS, B. B. 1993 Behaviour of meandering two-stage channels. *Proc. ICE Wat., Marit. and Energy* **101**, pp. 99–111.

SHIONO, K. & KNIGHT, D. W. 1989 Vertical and transverse measurements of Reynolds stress in a shear region of a compound channel. *Proc. 7th Intl Symp. on Turbulent Shear Flows*, August, pp. 28.1.1–28.1.6. Stanford University, USA.

SHIONO, K. & KNIGHT, D. W. 1991 Turbulent open-channel flows with variable depth across the channel. *J. Fluid Mech.* **222**, 617–646 (and **231**, 693).

SHIONO, K. & MUTO, Y. 1993 Secondary flow structure for in-bank and over-bank flows in trapezoidal meandering compound channel. *Proc. 5th Intl Symp. on Refined Flow Modelling and Turbulence measurements*, 7–10 September, pp. 645–652, Paris, France.

SHIONO, K., MUTO, Y., IMAMOTO, H. & ISHIGAKI, T. 1994 Flow structure in meandering compound channel for overbank. *Proc. 7th Intl Symp. Application of Laser Techniques to Fluid Mechanics*, 10–14 July, pp. 28.2.1–28.2.8. Lisbon, Portugal.

SHUKRY, A. 1950 Flow around bends in an open flume. *Trans. ASCE* **115**, 751–779.

STEIN, C. J. & ROUVÉ, G. 1988 2D-LDV-technique for measuring flow in a meandering channel with wetted flood plains – A new application and first results. *Proc. Intl Conf. on Fluvial Hydraulics*, pp. 5–10. Budapest.

TAMAI, N., ASAEDA, T. & IKEDA, H. 1986 Generation mechanism and periodicity of large surface-eddies in a compound channel flow. *Proc. 5th Congress APD-IAHR*, pp. 61–74. Seoul, Korea.

TOEBES, G. H. & SOOKY, A. A. 1967 Hydraulics of meandering rivers with floodplains. *J. Waterways Harbors Div., Proc. ASCE* **93**, WW2, 213–236.

TOMINAGA, A. & NEZU, I. 1991 Turbulent structure in compound open-channel flows. *J. Hydraul. Engng* **117**, 21–41.

UTAMI, T. & UENO, T. 1991 Experimental study on the compound meandering channel flow using flow visualization and picture processing. *J. Hydrosci. Hydraul. Engng* **9**, 1–10.

WILLETTS, B. B. & HARDWICK, R. I. 1993 Stage dependency for overbank flow in meandering channels, *Proc. ICE Wat., Marit. and Energy* **101**, 45–54.

ZHELEZNYAKOV, G. V. 1965 Relative deficit of mean velocity of unstable river flow, kinematic effect in river beds with flood plain. *Proc. 11th IAHR Congress*. Leningrad.